

Advancing interpretation of incoherent scattering in ice penetrating radar data used for ice core site selection

Ellen Mutter¹ and Nicholas Holschuh²

¹Department of Earth and Atmospheric Sciences, Cornell University, Ithaca, NY, 14853, USA

²Department of Geology, Amherst College, Amherst, MA 01002, USA

Correspondence to: Nicholas Holschuh (nholschuh@amherst.edu)

Abstract. Below the coherent layering in ice penetrating radar data collected in Antarctica and Greenland, incoherent scattering is common. This scattering is signal, not noise, and has the potential to inform our understanding of the structure and dynamics of the bottom 20% of glaciers and ice sheets. Here, we present a comparison between radar imagery and ice core properties for ~~sixteen~~ ice core sites across Antarctica and Greenland, to identify possible sources for incoherent scattering and evaluate its use in ice core site selection. We find that incoherent scattering is commonly coincident with either gradual changes in crystal orientation fabric or rapidly fluctuating fabrics in deep ice, where strain is localized by strength differences associated with ice grain size. Macro-scale deformation and layer folding at scales below the range-resolution of radar does not seem to result in incoherent scattering or induce an echo free zone, as has been previously hypothesized. Where incoherent scattering is laterally homogeneous in intensity, layering is typically undisturbed in nearby ice cores. But where incoherent scattering is laterally heterogeneous in intensity and the pattern does not appear conformal with subglacial topography, we find multi-meter-scale folding and associated discontinuities in nearby ice core records. Future higher-resolution sampling of fabric in ice cores would allow for more quantitative interpretation of incoherent scattering and its amplitude, but we show that the qualitative nature of incoherent scattering has the potential to inform us about the continuity of climate records at prospective ice core sites and should be considered when evaluating the nature and quality of basal ice.

Deleted: seventeen

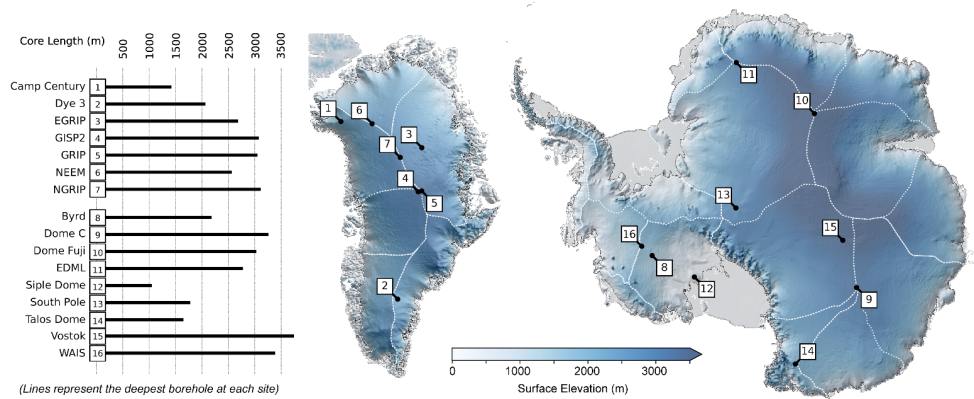
1. Introduction

Existing ice cores provide our best record of past atmospheric chemistry. These cores capture global climate changes over the Holocene and Late Pleistocene (Wolff et al., 2010). Future ice coring initiatives hope to build on that record, both extending it further back in time (Jouzel and Masson-Delmotte, 2010) and measuring regional climate change (Mulvaney et al., 2021) during specific climate periods (Fudge et al., 2023). These future projects focus on the identification and collection of very specific ice, and so they typically start with extensive geophysical surveying for “site selection” preceding drilling. Ice penetrating radar data have served as the primary tool for this work, which uses layering in radar imagery to infer spatially variable accumulation, basal melting, and ice flow, and through that, identifying ideal ice core sites (Bingham et al., 2024; Chung et al., 2023; Karlsson et al., 2018; Schroeder et al., 2020). But site selection has relied primarily on the strong, coherent signal that spans the upper three-quarters of the ice column in most radar imagery. Here we focus on improving interpretation

33 of other signals in radar data, with a particular focus on what deep incoherent scattering (described in section 2) can tell us
34 about ice near the ice sheet base.

35 All radio-wave scattering in ice originates from dielectric contrasts. To better understand the nature and sources of scattering
36 in existing ice penetrating radar data, several previous studies have compared radar imagery to observations of ice chemistry
37 and physical properties measured in ice cores (e.g., Eisen et al., 2003, 2007; Hammer, 1980; Harrison, 1973; Millar, 1982;
38 Mojtabavi et al., 2022). But that work has focused on the coherent, isochronal layering, and comparatively little has been done
39 to understand the deeper signals, which are becoming better sampled with modern, high power / low noise systems. This deep
40 ice has also become increasingly scientifically important, as it is at the center of the search for an ice core record that spans
41 the Mid-Pleistocene transition (Chung et al., 2023; Lilien et al., 2021). Using data from 16 deep ice cores across Antarctica
42 and Greenland (Fig. 1), we work to better understand the physical properties that produce deep, incoherent scattering, and
43 evaluate the extent to which it may be diagnostic of layer disturbances or other disqualifying characteristics when pursuing
44 future ice cores.

Deleted: 17



45
46 **Figure 1: Locations of deep ice coring initiatives in Greenland and Antarctica used in this study and the lengths of the associated**
47 **cores. Surface elevation maps of Antarctica (Howat et al., 2019) and Greenland (Porter et al., 2018) with catchment boundaries**
48 **(Mouginot and Rignot, 2019; Rignot et al., 2013) showing ice divides in white.**

Deleted: major

2. Background: Scattering and the Radar Imaging Problem

Radar systems actively transmit energy into the subsurface. Time-of-flight measurements for back-scattered energy (together with a known speed of light in ice) can be used to infer the position of subsurface scatterers and reconstruct the geometry of glacier systems (Bingham et al., 2024; Dowdeswell and Evans, 2004). In the near sub-surface, contrasts in the dielectric permittivity that scatter energy are controlled primarily by variations in density, while most deeper englacial reflectors arise from either conductivity contrasts, due to variations in the concentration of free ions deposited with the snow at the surface (Stillman et al., 2013), or transitions in the ice crystal fabric, typically localized by changes in grain size also arising from impurity deposition (Fujita et al., 1999). Fabric induced scattering is a product of the dielectric anisotropy of individual ice crystals, with transitions in c-axis fabric capable of producing an (up to) $\sim 1.3\%$ contrast in the polarization-dependent bulk permittivity (Matsuoka et al., 1997). Incoherent scattering may come from both chemical and physical sources; we work to provide some of the first constraints on its origins here.

Glaciologists primarily use radar data for ice core site selection in two ways. The first approach is focused on the geometry of coherent, isochronous layering within the ice sheet (an example of which can be seen in the upper portions of Fig 2.a). These layers originate as flat-lying layers of snow at the ice sheet surface and are transformed by flow during burial; thus, their geometry can be used to diagnose spatial variations in accumulation (e.g., Karlsson et al., 2020), glacier sliding (e.g., Leysinger Vieli et al., 2007), and basal melt (e.g., Bingham et al., 2024; Fahnestock et al., 2001). The second approach is focused on the nature of subsurface scattering, both its coherence (e.g., Lindzey et al., 2020; Oswald et al., 2018; Schroeder et al., 2015) and amplitude (e.g., Catania et al., 2003; Christianson et al., 2016; Chu et al., 2018), which together can be used to infer the modern electrical (and, more generally, material) characteristics of the ice sheet and its substrate.

Subsurface targets can be divided into two main categories: specular interfaces and rough (or diffuse) scatterers (Schroeder et al., 2015). Specular interfaces, like mirrors, scatter energy in one dominant direction, a function of the direction-of-arrival for the incoming radio wave and the orientation of the interface. Diffuse scatterers redistribute incident energy at a variety of angles. This leads to significant differences in the coherence of the scattering between specular and diffuse targets (defined here as the consistency in phase and amplitude of the backscattered energy with slight changes in the position of the radar system). Incoherent scattering typically occurs at rough interfaces or when there are multiple diffuse scattering targets at a similar range from the instrument. It has been observed as a product of rare glacier conditions, for example, where there is significant temperate ice and associated englacial water (Hamran et al., 1996) or where debris has been entrained near the base of glaciers (Winter et al., 2019). But it must also be generated by more common glaciological phenomena, as it is present within several hundred meters of the ice sheet base across large parts of Antarctica and Greenland.

Consider the example radar image in Fig. 2.a. Each pixel represents either backscattered energy or electrical or thermal noise in the radar electronics. The position of the radar system varies across the columns in the image, and the delay-time following the transmitted pulse (associated with the range to possible targets) varies across the rows in the image. In regions dominated by planar, specular interfaces (as in the upper half of Fig. 2.a), each pixel typically represents backscattered energy from only a single direction of arrival. This is because, even though there are many scattering targets at the range associated with that pixel (as shown in Fig. 2.b), only that interface tangential to the range shell (such that the interface is normal to the propagating wave) returns energy to the system. But in regions where there are diffuse scatterers, each pixel in a radar image represents the interference of scattering from multiple targets, with backscattering arriving from multiple angles (Fig. 2.b.ii/iii). With slight changes in the position of the system, the dominant source of scattering at a given range can change, resulting in little consistency in phase or amplitude from pixel to pixel. This is extremely common for energy arriving below the ice bottom reflector, with a long tail of incoherent scattering appearing at greater range (Fig. 2.a.iii). Less well described is incoherent scattering from within the ice column (Fig. 2.a.ii) which is the focus of our research here.

When considering the nature of scattering in radar imagery, it is important to remember that the images themselves are ultimately a product of three things:

1. The geometry and physical / electrical characteristics of the glacier subsurface.
2. The system used to collect the data (including the characteristics of the transmitted wave, antennas, and transmit / receive electronics).
3. The filtering, focusing, and additional image processing algorithms applied after collection.

The nature of radar targets depends on both the scale of electromagnetic heterogeneity in the medium and the frequency content of the transmit pulse (with higher frequencies / bandwidths associated with finer range resolution). This is because the specularity of a target is ultimately dictated by the Rayleigh roughness criterion for an interface, with specular scattering occurring when roughness elements are less than $1/8^{\text{th}}$ the scale of the dominant radar wavelength (Peters et al., 2005). Figure 2.c demonstrates how the same targets manifest differently across different radar systems; with lower resolution systems, scattering appears more structured, like the specular and coherent layering in the shallow ice.

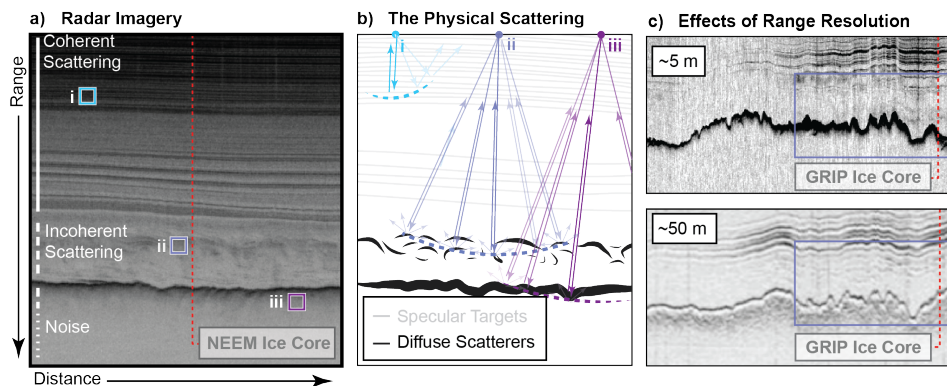


Figure 2: (a) Example radar image, (b) the ray-paths associated with scattering targets that contribute to individual pixels in the radar imagery, and (c) a pair of images highlighting the effect of system characteristics on the nature of deep scattering. Profiles presented in panel (c) were collected along sub-parallel tracks adjacent to the GRIP Ice Core site. Radar system characteristics for radargrams in (a) and (c) can be found in Supplementary Table 1.

To generate incoherent scattering, deep ice must differ from the planar, layered structure of the shallow ice column in some way. It may be that incoherent scattering occurs because chemical layering is mechanically disturbed in the deep ice and is no longer planar. Or, it may be that other processes (like dynamic recrystallization or grain rotation) acting locally (due to enhanced stress near obstacles to flow, transitions in the basal thermal state, or fluidity contrasts in the ice) introduce lateral heterogeneity in physical properties that produce incoherent scattering (Gerber et al., 2024). Here, we compile radar data from a variety of geophysical campaigns, including ground-based and airborne surveys conducted by the Center for Remote Sensing and Integrated Systems (CReSIS), the British Antarctic Survey (BAS), the University of Texas (UT), the University of Washington (UW), and the Alfred Wegener Institute (AWI) – (see Supplementary Table 1 for full system characteristics). From those data, we analyze representative, ice core adjacent radar images, and compare them to measurements of crystal orientation fabric and micro- and macro-scale structures, to test two hypotheses:

1. That transitions in ice COF are collocated with (and likely induce) incoherent scattering.
2. That small scale deformation of chemically distinct layering can induce incoherent scattering.

We are drawing from heterogeneous, historical data, which can make imagery intercomparison difficult. Because some systems used for site selection do not preserve phase information, we focus primarily on the amplitude and character of scattering, controlling for differences in system characteristics. Differences in image processing also have the potential to modify the expression and amplitude of incoherent scattering. Therefore, an important caveat of this work is that our interpretation of incoherent scattering only holds for imagery collected with radar hardware typical of the earth 2000's (with center frequencies in the 100s of MHz) and the most common image post-processing (SAR focusing and along-track multilooking).

Deleted:

132 **3. Data and Methods: Measurements Capturing the Fine- and Large-Scale Electrical Structure of Ice Cores**

133 Folds and layer disturbances at all scales have been observed or inferred from ice core records in both Antarctica and
134 Greenland. Some scales of folding are more easily detected – millimeter and centimeter scale folds can be measured directly
135 within the 8-13 cm diameter ice cores. Folding at the 100s of meters scale is resolvable by radar. But all scales in between
136 must be inferred using anomalous patterns of electrical conductivity, stable isotope or impurity concentrations, or physical and
137 optical properties. We summarize the measurements that we use to identify deformation in deep ice below, and aim to relate
138 radio-wave scattering phenomena to these observations.

139
140 Physical analysis of ice cores, including macro-scale visual observations and optical imaging (i.e. linescanners) (Faria et al.,
141 2018; Jansen et al., 2015; Svensson, 2005), and alternating current and direct current electrical conductivity measurements
142 (ECM) (Fudge et al., 2016; Wolff, 2000) provide the best direct measurement of small-scale features deep in the ice column.
143 The resolution of typical linescan images is around 0.1 mm/pixel, allowing for observations of layers and their structure ranging
144 from millimeter-scale undulations up to folds at the scale of the typical diameter of deep ice cores (Fig. 3). Data from ice core
145 linescanning have shown wavy strata (e.g. WAIS -- West Antarctic Ice Sheet Divide (Fitzpatrick et al., 2014)), highly inclined
146 strata (e.g. EDML -- EPICA Dronning Maud Land (Faria et al., 2018)), duplex and boudin-like structures (e.g. EastGRIP
147 (Westhoff, 2021)), 10 cm-scale z-folds (e.g. NEEM -- North Greenland Eemian Ice Drilling (Jansen et al., 2015)), diffuse
148 layering (e.g. NorthGRIP (Svensson et al., 2005)), and extreme growth of individual ice grains reaching diameters of up to 50
149 cm (e.g. EDML (Faria et al., 2018)), capturing unique forms of stratigraphic disturbance and in some cases, informing the
150 depth associated with discontinuities in the climate record (Fig. 4).

151
152 To supplement imaging methods that capture small scale deformation, a range of chemical methods have been employed across
153 deep ice core sites to identify major breaks in stratigraphic continuity and large-scale folding. Some breaks in continuity have
154 been identified using chemical disagreement between ice cores. For cores in the same geographic region (e.g. GISP2 --
155 Greenland Ice Sheet Project Two, GRIP -- Greenland Ice Core Project, and NorthGRIP -- North Greenland Ice Core Project),
156 divergence in electrical conductivity, $\delta^{18}\text{O}$ of ice ($\delta^{18}\text{O}_{\text{ice}}$), and impurity concentrations can be used to identify the onset of a
157 discontinuous record (Johnsen et al., 2001). When looking across hemispheres, divergence in the profiles of globally well-
158 mixed $\delta^{18}\text{O}$ of atmospheric O_2 ($\delta^{18}\text{O}_{\text{atm}}$) and CH_4 have been used to identify climate record discontinuity (Chappellaz et al.,
159 1997; Landais et al., 2003). In cases where there are no cores that provide high resolution comparison, sudden shifts in the
160 nature of the chemical signal (e.g. changes in chemical variability or abrupt changes in the gas-age ice-age difference, described
161 as either the Δage between the ice and gas or the depth-shift separating gas and ice of a constant age) have been used to infer
162 climate record discontinuities (Crotti et al., 2021; Dansgaard, 1982; Jouzel et al., 2007; Petit et al., 1999; Ruth et al., 2007).
163 Chemical methods have also been used to reconstruct chronologies in heavily disturbed stratigraphy (Landais et al., 2003;

164

Deleted:

Deleted: ¶

Figure 3: Examples of linescan images capturing mm to >10-cm scale deformational structures. Microinclusion-rich ice strata scatter light creating bright horizons, or cloudy bands, revealing stratigraphic structure. Well-defined planar layering with mm-scale undulations is observed in all cores with available linescan images. Cm-scale deformational structures include z-folds (EDML and GISP2), cm-scale undulations (NEEM and NorthGRIP), and boudin-like structures (EastGRIP). Overturning folds that span over 10 cm of the ice column are observed at EDML and NEEM. Ice without layer structure can be due clear ice that lacks sufficient microinclusions for scattering (NEEM and EastGRIP) as well as ice with large individual crystal grains (EDML and NorthGRIP). Diffuse or weak layering is observed when microinclusions are minimal (NEEM and EastGRIP) or lacking clear layer structure (NorthGRIP). Linescan data is sourced from Faria et al., 2018 (EDML), Takata et al., 2004 (Dome Fuji), Kipfstuhl, 2009 (NEEM), Svensson, 2005 (NorthGRIP), Alley et al., 1997 (GISP2), Weikusat et al., 2020 (EastGRIP). ¶

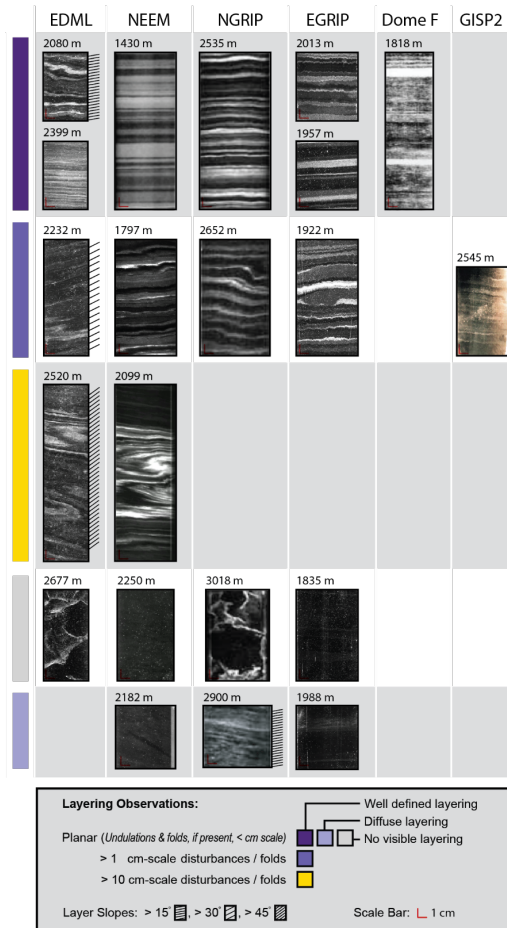


Figure 3: Examples of linescan images capturing mm to >10-cm scale deformational structures. Microinclusion-rich ice strata scatter light creating bright horizons, or cloudy bands, revealing stratigraphic structure. Well-defined planar layering with mm-scale undulations is observed in all cores with available linescan images. Cm-scale deformational structures include z-folds (EDML and GISP2), cm-scale undulations (NEEM and NorthGRIP), and boudin-like structures (EastGRIP). Overturning folds that span over 10 cm of the ice column are observed at EDML and NEEM. Ice without layer structure can be due clear ice that lacks sufficient microinclusions for scattering (NEEM and EastGRIP) as well as ice with large individual crystal grains (EDML and NorthGRIP). Diffuse or weak layering is observed when microinclusions are minimal (NEEM and EastGRIP) or lacking clear layer structure (NorthGRIP). Linescan data is sourced from Faria et al., 2018 (EDML), Takata et al., 2004 (Dome Fuji), Kipfstuhl, 2009 (NEEM), Svensson, 2005 (NorthGRIP), Alley et al., 1997 (GISP2), Weikusat et al., 2020 (EastGRIP).

197 NEEM Community Members, 2013; Raynaud et al., 2005; Souchez et al., 2002; Verbeke et al., 2002), and from those
198 chronologies, identify overturned folding. These methods have in some places tentatively inferred (e.g., at Vostok and GRIP)
199 and in other places clearly identified (at NEEM) folding on scales of 10-100 m.

200
201 In our analysis, we synthesize the literature on macro-scale stratigraphic disturbances, grouping and analyzing the effect of
202 deformational structures on radar scattering based on reported fold size, slope inclination, and layer visibility. To do this, we
203 identify the depth at which these features are observed (presented in Fig. 4) and compare the observed deformation patterns
204 with collocated radar imagery. Most studies present examples of deformational feature types followed by qualitative
205 descriptions of their frequency throughout the ice column; therefore, the reported ranges should be treated as zones of
206 deformational structures with intermittent occurrence, rather than a continuous span of small-scale deformation.

207
208 In addition to measurements capturing the macro-scale, we present crystallographic analysis of glacial ice, typically performed
209 using vertical and / or horizontal thin sections of ice cores. C-axis orientation can be measured with a range of techniques,
210 including polarized light microscopy (Azuma et al., 1999; Weikusat et al., 2017; Wilson et al., 2003), x-ray diffraction and
211 tomography (Miyamoto et al., 2011), sonic wave methods (Klusiewicz et al., 2017), electron backscatter diffraction
212 microscopy (Obbard and Baker, 2007), and open resonator methods (Saruya et al., 2024). Measurements of the bulk c-axis
213 orientation of glacial ice gives us a direct constraint on how the polarization-dependent permittivity of ice might vary with
214 depth, and therefore how variations in crystal orientation itself may be a source of scattering. C-axis measurements also provide
215 information about the strain history of ice, with implications for larger-scale deformation in the ice column.

216
217 Historically, data from thin sections have provided the most robust evidence of differential strain at small scales, capturing
218 fabric changes within a single 10 cm vertical thin section (e.g. NEEM (Montagnat et al., 2014)). But the logistics of thin section
219 sampling limits their ability to capture some scales of vertical and horizontal variability in fabric. The distance between
220 adjacent, discrete thin-section samples can be anywhere from 20 to 100+ m (e.g. EDML (Weikusat et al., 2013), Siple Dome
221 (Gow and Meese, 2007), NorthGRIP (Wang et al., 2002), GRIP (Thorsteinsson et al., 1997)). New approaches to c-axis
222 characterization may change what is possible in future studies of fabric derived scattering, as thick-section open resonator
223 methods have been used to measure the clustering of crystal c-axes every 20 mm along the Dome Fuji core (Saruya et al.,
224 2022, 2024). But for most available data, we are limited in our ability to quantitatively predict scattering from existing fabric
225 measurements, as the magnitude of backscatter depends on the depth-rate-of-change of fabric. Instead, we focus primarily on
226 qualitative comparison of fabric changes with radar images.

227

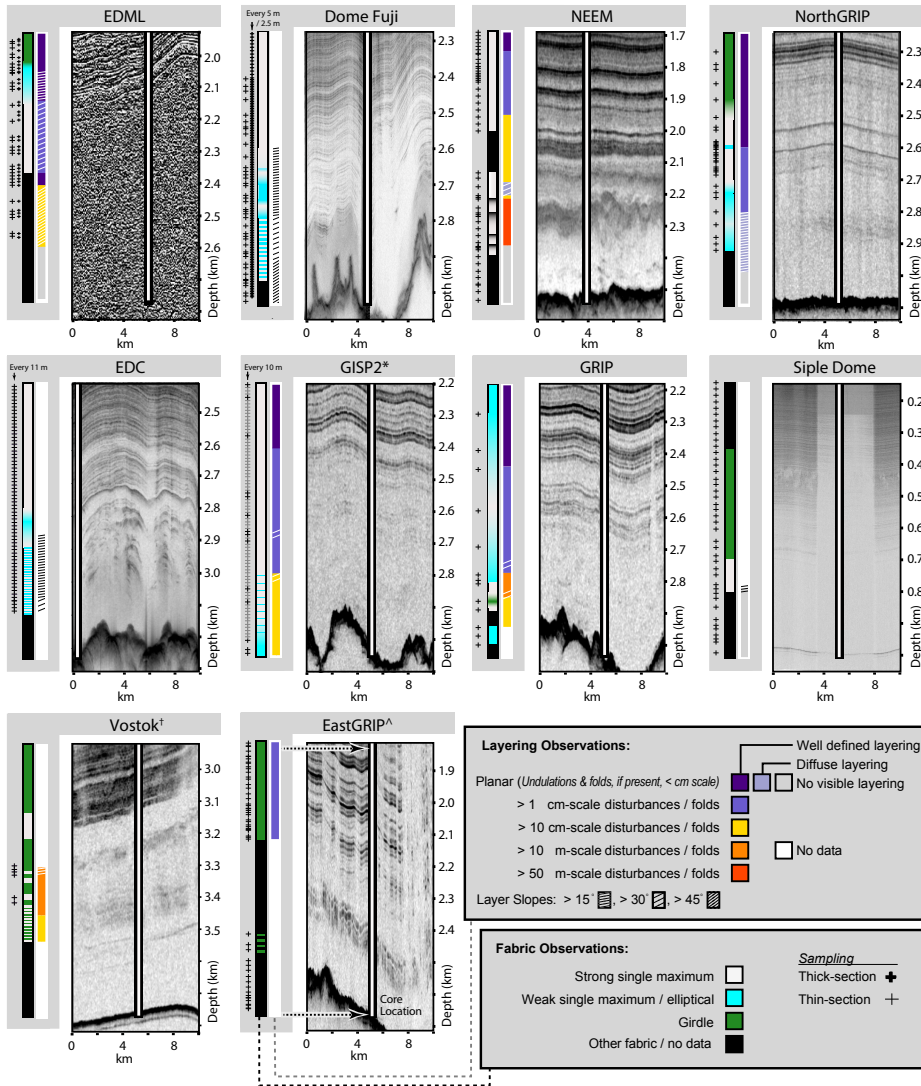
228 **3. Results: Investigating the Sources of Incoherent Scattering**

229 We present measured fabric and structural data together with radar imagery across 10 well sampled cores in Figure 4. We
230 encourage readers to refer to Figure 4 often as we describe the relationships between structural data and the radiostratigraphy
231 throughout section 3. In section 3.1, we evaluate the depth-agreement of scattering and known fabric transitions. In section
232 3.2, we evaluate the effect of small- and large-scale deformational structures on radar scattering. A full description of the ice
233 core data used to generate Figure 4 can be found in Supplementary Table 2.

234 **3.1 Crystal fabric transitions as a source of incoherent scattering**

235 Given the enhanced stresses and therefore higher strain-rates near the base of ice sheets, one might expect monotonic but
236 intensifying fabric development with depth. And at the majority of ice core drill sites, c-axis fabrics transition from a quasi-
237 isotropic c-axis distribution at the top of the ice column to a strong single maximum lower in the column (e.g. Camp Century,
238 Dye-3, GISP2, NEEM, EPICA Dome C (EDC), Talos Dome, GRIP), a product of the typical simple shear near the base of a
239 glacier. Ice cores drilled at flank sites or otherwise away from ice divides often exhibit signs of uniaxial horizontal extension,
240 and thus c-axis fabrics transition from quasi-isotropic to girdle-type fabric and then to a single maximum (e.g. NorthGRIP,
241 Vostok, EDML). But variability in the impurity content (which changes with climate) can intensify fabric development and
242 localize fabric transitions, with fabric strengthening typically coincident with higher impurity content (seen at Byrd (Faria et
243 al., 2014), Camp Century (Faria et al., 2014), Talos Dome (Montagnat et al., 2012), EDC (Durand et al., 2009), NEEM
244 (Montagnat et al., 2014), GISP2 (Gow et al., 1997), and Dye-3 (Langway et al., 1988)).

Deleted: ,
Deleted: and w
Deleted: of



Deleted:

251 Figure 4: Radargrams capturing deep ice at ice core drill sites with comprehensive fabric and stratigraphic deformation data. From
252 left to right, each ice core panel presents a scatter plot marking sample depths where thin sections, and thick sections where
253 applicable, were collected for crystal orientation fabric analysis, a colormap visualizing of fabric evolution with depth, a colormap
254 visualizing layering evolution and layer slope observations with depth, and a 10 km length radar transect proximal to the ice core
255 drill site. Fabric observations categorized as “other fabric” include multimaxima fabrics (e.g. at EastGRIP and NEEM).
256 Radargrams span the bottom 850 m of each core and 50 m of bedrock. Backscatter power color scales are standardized to span 0.5%
257 to 99% of the return power amplitude recorded in the presented depth range. Radar system characteristics can be found in
258 Supplementary Table 1. The synthesized ice core data includes fabric observations: EDML (Eisen et al., 2007; Faria et al., 2018;
259 Weikusat et al., 2013), Dome Fuji (Saruya et al., 2022, 2024), NEEM (Eichler, 2013; Montagnat et al., 2014), NorthGRIP (Wang et
260 al., 2002), EDC (Durand et al., 2009), GISP2 (Gow et al., 1997), GRIP (Thorsteinsson et al., 1997), Siple Dome (Gow and Meese,
261 2007), Vostok (Obbard and Baker, 2007), EastGRIP (Stoll et al., 2024); and layering observations: EDML (Faria et al., 2010, 2018),
262 Dome Fuji (Dome Fuji Ice Core Project Members, 2017), NEEM (Jansen et al., 2015), NorthGRIP (Svensson, 2005), EDC (Durand
263 et al., 2009), GISP2 (Alley et al., 1995, 1997; Faria et al., 2014; Gow et al., 1997), GRIP (Alley et al., 1995; Dahl-Jensen et al., 1997;
264 Johnsen et al., 1995; Landais et al., 2003), Siple Dome (Gow and Meese, 2007), Vostok (Lipenkov and Raynaud, 2015; Raynaud et
265 al., 2005; Souchez et al., 2002), EastGRIP (Westhoff, 2021; Stoll et al., 2023). *At GISP2, only some of the sampled thin sections have
266 published data (indicated by the black + symbols), and ^at Vostok, the original sampling rate is unpublished, with only a few thin
267 sections and general observations available in the literature. ^At EastGRIP, visual characterization of cloudy bands combines folded
268 features and weak layering into a single group (Stoll et al., 2023). We review the published linescan images at EastGRIP and present
269 approximate depths of these two types of layering in Fig. [S1](#).

270
271 Abrupt fabric transitions occur within most ice cores in Greenland (e.g. Camp Century, Dye-3, GISP2, and NEEM), where a
272 significant change in impurity deposition at the Holocene-Wisconsin climate transition drives an abrupt strengthening or
273 transition to a vertical-maximum fabric (Faria et al., 2014). In some places, we see a co-located scattering horizon associated
274 with these abrupt transitions in fabric. At NEEM, a transition from a weak vertical girdle to strong single maximum fabric
275 occurs at 1419 m and is coincident with a diffuse reflector in the radargram (Fig. [S2](#)). Similar reflectors appear at isolated
276 fabric transitions in Antarctica as well. At Siple Dome, the c-axis fabric transitions from a vertical girdle to a single maximum
277 at 700 m, with a corresponding diffuse reflector in the radar data. At EDML, the c-axis fabric transition from a vertical girdle
278 to a strong single maximum between 2025 m and 2045 m has been identified as the origin of the reflector at 2035 m (Eisen et
279 al., 2007). These reflectors appear less specular (with trailing energy after the initial arrival) than other isochronous layering
280 within radar imagery.

281
282 Where we see well sampled gradual transitions in fabric (spanning 50-100 m of the ice column) we observe both diffuse bands
283 of incoherent scattering as well as laterally heterogeneous incoherent scattering. At EDC, the strong single maximum fabric at
284 2800 m gradually transitions to a broad single maximum fabric at 2857 m and returns to a strong single maximum fabric at
285 2900 m (Durand et al., 2009). This fabric transition is roughly coincident with the transition from coherent isochronal strata to
286 a single diffuse incoherent scattering layer observed around 2825 m. At Dome Fuji, the strong single maximum fabric at 2660
287 m gradually weakens before returning to a strong single maximum fabric again at 2760 m (Saruya et al., 2024). This fabric
288 transition appears roughly coincident with a weak diffuse incoherent scattering layer observed at ~2700 m in the radargram
289 (Fig. [S3.a](#)).

Deleted: S
Deleted: 4

Deleted: S1

Deleted: S2

295 In many places, especially where annual layer thickness is compressed significantly at the base of the ice column, alternating
 296 fabrics have been observed. At Vostok, from 2700 to 3315 m depth, the core alternates between coarse-grained ice with girdle-
 297 type fabric and fine-grained ice with single-maximum fabric every ~100 m (Obbard and Baker, 2007). Within the girdle-type
 298 fabric zone between ~3220 and 3315 m, we see weakly banded incoherent scattering (3220 – 3290 m). Between ~3315 and
 299 3450 m, alternations between girdle-type and single-maximum fabric occur approximately every ~20 m (Lipenkov and
 300 Raynaud, 2015). This zone of increased fabric alternation overlaps with both the no echo zone between ~3290 and 3360 m
 301 and the upper depths of a weakly banded incoherent scattering unit (~3360 – 3490 m) in the radargram. At GRIP, each of the
 302 five thin sections sampled between 2800 and 2950 m depth show alternating fabrics. At GISP2, coarse-grained layers with
 303 fabrics that deviate from the strong single maximum are observed at increasing frequencies below 2800 m (Gow et al., 1997).
 304 While interpretation of the GISP2 and GRIP radargrams is challenging below 2800 m, 35 km length radar transects show
 305 laterally heterogeneous incoherent scattering in that depth range (Fig. S4).

Deleted: S3

307 While it is challenging to describe fabric variability at all scales from thin-sections due to their irregular sampling frequency,
 308 the smallest scale of fabric variability has been observed or inferred at centimeter-scales, including at Vostok, EDC, Dome
 309 Fuji, and EastGRIP.

- 310 • At Vostok, fabric alternations occur at cm-scale wavelengths from 3450 m until the transition from meteoric to
 311 accreted ice at 3538 m (Lipenkov and Raynaud, 2015). This overlaps with an echo-free zone in the radargram.
- 312 • At EDC, ice below 2800 m consists of alternating layers with high impurity content (consistently presenting strong
 313 single maximum fabric) and layers with low impurity content (with an associated broad single maximum fabric).
 314 After the gradual transition into and out of a broad single maximum fabric at 2850 m, fabric transitions below 2920
 315 m become more local. High spatial sampling (every 0.5 m) between 2933 and 2955 m revealed fabric alternations
 316 between each sample (Durand et al., 2009). Unlike at Vostok where the onset of rapid fabric transitions coincides
 317 with the start of the echo free zone, the onset of rapid fabric transitions at EDC is associated with thick and sometimes
 318 discontinuous bands of incoherent scattering (2900 – 3050 m) in the radargram.
- 319 • At Dome Fuji, cm-scale fluctuations from the single maximum fabric, observed by increases in the standard deviation
 320 of $\Delta\epsilon$ (the difference in the relative permittivity, ϵ , between vertical and horizontal planes), begin around 2400 m and
 321 intensify through the base of the ice column (Saruya et al., 2024). The increase in fabric fluctuations between 2400
 322 and 2650 m has no obvious effect on the coherent continuous layering observed in the radargram. However, the Dome
 323 Fuji radargram transitions to a zone of laterally homogenous incoherent scattering at 2900 m. Notably, the precise
 324 depth of that transition is difficult to constrain in the radar image, due to the combination of increasing layer
 325 inclinations (Dome Fuji Ice Core Project Members, 2017) and strong scattering from borehole fluid in the ice core
 326 cavity (Fig. S3).
- 327 • At EastGRIP, rapid transitions between vertical girdle and multi-maximum fabrics are observed between 2417 and
 328 2484 m, with a strong multi-maximum fabric established below 2500 m (Stoll et al., 2024). The depth range of the

Deleted: S2

rapid fabric transitions coincides with a layer-conformal package of incoherent scattering. Banding within the package of incoherent scattering is not layer-conformal, and the bands are defined by laterally traceable, abrupt drops in power with depth (rather than laterally traceable, abrupt increases in returned power as we see in the coherent layering above). We describe these traceable lows in power as “nulls”, likely the product of destructive interference in scattered energy returning to the radar from multiple directions. The expression of the nulls in the imagery is polarization dependent (Fig. S1; Nymand, 2024 Fig. 3.5) suggesting that this entire scattering package is a result of the fabric.

At NEEM, four sequences of abrupt and then gradual fabric transitions are linked to large-scale deformation starting at ~2200 m. In this section of the ice core, the same oxygen isotope sequence (and its associated fabric gradient, from multi-maxima fabric to single maximum fabric) is repeated, with abrupt fabric transitions at the boundaries between sequences. This is attributed to overturned folds at the base of the ice column, in part, facilitated by rheologic differences in the ice that also produce the abrupt fabric transitions. At these depths we see strong incoherent scattering that is highly laterally variable. Here, both fabric and larger-scale deformation likely play a significant role in the nature of the scattering, with folding introducing lateral heterogeneity in material properties that has not been identified at other ice core sites.

3.2 Folding as a source of incoherent scattering

Millimeter-scale disturbances are likely present in most deep glacial ice, given their ubiquity in ice cores. But we find little evidence that deformation at that scale impacts the radiostratigraphy directly. In the South Pole Ice Core (SPICEcore), inclined and pinched cloudy bands are observed starting at 1000 m and continue intermittently through the end of the core (Fegyveresi and Alley, 2018) without any noticeable impact on radar scattering. Crystal striping at GISP2 is observed starting at 2200 m, coincident with the onset of small-scale undulations in linescan images (Alley et al., 1997). But similar to SPICEcore, there is no associated change in the nature of radar layering. Millimeter-scale z-folds at GRIP first appear at 2438 m and at 2437 m at GISP2 (Alley et al., 1997), which does coincide with a drop in power of coherent scattering layers. But there is a commensurate drop in the ice conductivity variability associated with changes in dust deposition, which better explains that change. Thus, we rule out millimeter-scale folding as a significant contributor to the radar signal observed at these locations.

Stratigraphic disturbances at the centimeter-scale are apparent in all cores with available data. In previous work, this scale of deformation has been invoked as a mechanism for the “echo free zone”, with the idea that folding effectively homogenizes dielectric contrasts at the scale of the resolution of the radar (Winter et al., 2017). At EDML and WAIS Divide, the onset of cm-scale disturbance does appear to be collocated with the apparent echo free zone. In both radar images, however, there is a gradual diminution of returned power with depth. It is possible that measured disturbances do reduce the intensity of back-scatter without eliminating it entirely. But there is laterally-continuous layering (with strong back-scatter intensities) in regions of cm-scale disturbances at NorthGRIP, NEEM, EastGRIP, and GRIP, and in regions with disturbances at the scale of 10 cm

Deleted: s

Deleted: 4

365 at NEEM. Radar data at NEEM show no change in scattering behavior associated with deformation at this scale. This seems
366 to imply that these radar systems (with range-resolutions of 2.8 m to 5 m (Supplementary Table [1](#))) are insensitive to
367 deformation at this scale.

Deleted:

Deleted: S1

368
369 Larger scale folding does seem to have an effect on the radiostratigraphy. Deeper in the NEEM core, where chemical analyses
370 reveal six zones of disturbed ice, including two large 50 and 100 m thick folded layers of inverted early glacial ice (NEEM
371 Community Members, 2013), high amplitude but laterally variable incoherent scattering can be seen in the radar imagery.
372 Deformation at this scale, thought to be in part due to rheological differences between the glacial and interglacial ice (NEEM
373 Community Members, 2013), is coincident with a loss of coherent banding in the linescan imagery and an increase in the
374 lateral heterogeneity of intensity in incoherent backscatter. Above 3460 m depth at Vostok, folding is also inferred at the meter
375 scale and larger (Lipenkov and Raynaud, 2015). Similarly, there is incoherent scattering in the image at these depths, although
376 the amplitude of the backscatter is weaker, and lateral heterogeneity less pronounced. Finally, at GRIP, tentative chronological
377 reconstructions of disturbed ice below 2750 m show significant disruption and folding on the scale of 10s of meters between
378 2780 to 2850 m. And while near the ice core, this depth-range corresponds with a unit of weak incoherent scattering, at the
379 10s of kilometers scale, there is significant variability in the amplitude (Fig. [S4](#)).

Deleted: S3

380 **4. Discussion: Using Incoherent Scattering in Ice Core Site Selection**

381 There is compelling evidence that incoherent scattering can arise from fabric transitions in the deep ice, and the quality of that
382 scattering could be diagnostic of large-scale deformation that is co-located with the smaller-scale fabric development. If true,
383 then incoherent scattering might be used to improve ice core site selection. We test that theory at [16](#) ice core sites, by first
384 subdividing core-adjacent radar imagery into five types of signal (Figs. 5a and 5b):

Deleted: 17

- 385
- 386 1. Laterally continuous coherent scattering (that is, clear isochronal layering)
 - 387 2. Diffuse but banded scattering
 - 388 3. Laterally homogenous incoherent scattering
 - 389 4. Laterally heterogeneous incoherent scattering
 - 390 5. No signal (or rather, signal levels at or below the noise floor of the system).

391
392 We then compare these scattering types to known breaks in the continuity of the associated ice cores (see Appendix A for the
393 observational basis for each labelled break).

394
395 Across these core sites, continuous coherent scattering is almost exclusively found above known breaks in the climate record.
396 This type of scattering appears below the break in a climate record in only one ice core, and that is Vostok, where the interface

401 between accreted and meteoric ice and a layer of mineral inclusions from the lake bed (Turkeev et al., 2021) define two clear
402 reflection horizons. As a result, in typical glaciological environments, continuous coherent scattering is a robust indicator of
403 ice core continuity. At the studied core sites, where diffuse but banded scattering sits immediately below laterally continuous
404 layering (as is the case at EDC and EastGRIP), there are no associated breaks in measured climate records. This supports the
405 idea that banded but incoherent scattering is not an indication of disturbed basal ice.

406
407 Where we see laterally homogenous incoherent scattering, as in Camp Century, EDC, Dome Fuji, and NorthGRIP, it occurs
408 within sections of ice with a continuous climate record. This likely indicates fabric transitions that are themselves defined
409 weakly by depositional impurities, and thus, the shape of the scattering band is roughly parallel to the isochronous layering.
410 At Vostok, we see incoherent scattering that is laterally heterogeneous in its intensity but is otherwise layering conformal,
411 directly above and ~100 - 200 m below the broken climate record. These two bands of incoherent scattering are qualitatively
412 indistinguishable, and demonstrate the challenge of interpreting the quality of the climate record within regions characterized
413 by bed conformal laterally heterogeneous incoherent scattering.

414
415 But where we see laterally heterogeneous incoherent scattering that is layering non-conformal (as in GISP2, GRIP, and NEEM)
416 it occurs below breaks in the continuity of the observed climate record. We show that the source of the backscattering is
417 transition in the crystal fabric of the glacier, and its macro-scale expression comes from the nature of the vertical and lateral
418 heterogeneity in fabric. In those places, it is possible that the same ice rheology contrast that facilitated a fabric transition
419 interacts with the complex, local, basal stress regime to enable multi-meter scale deformation. This induces lateral variability
420 in the backscatter intensity, and can be taken as a significant risk for a disturbed climate record.

421

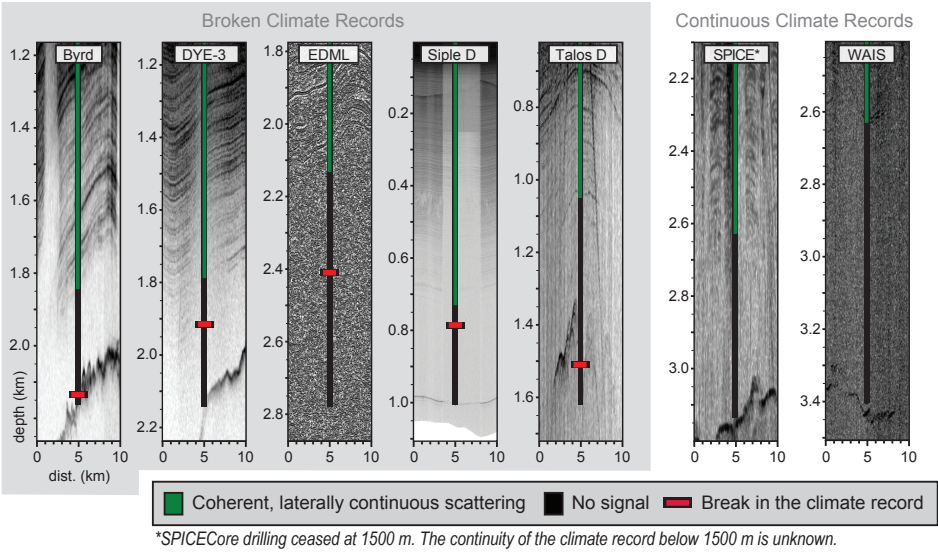
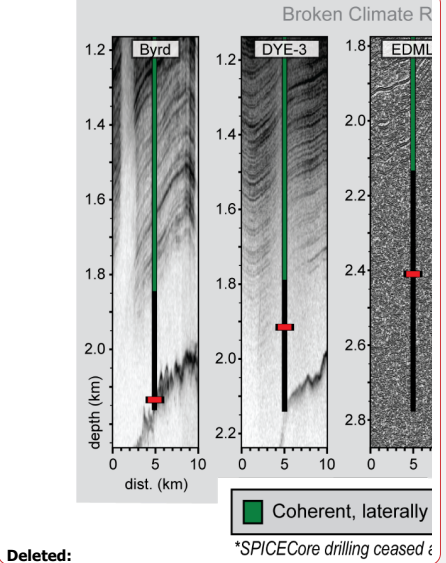


Figure 5a



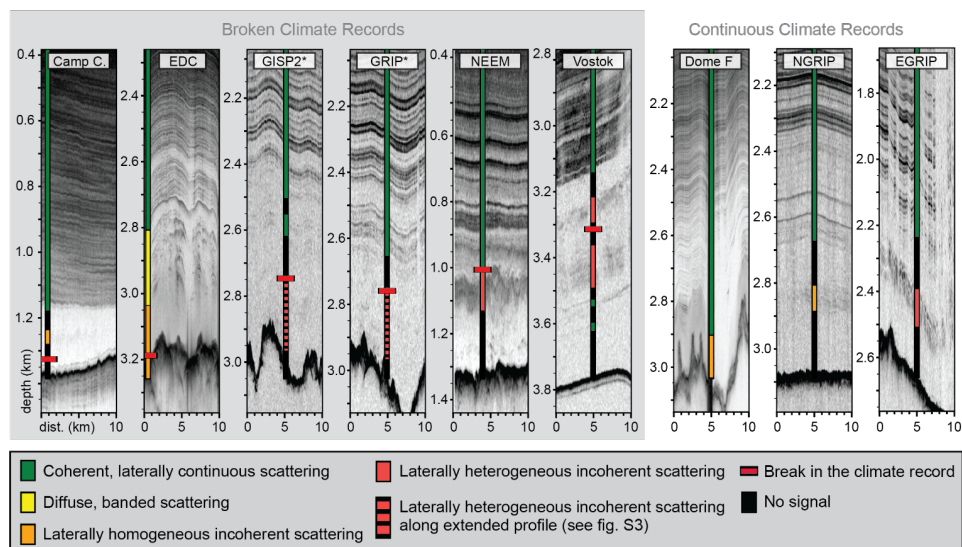


Figure 5b

Figure 5: 10 km length radar profiles collected proximal to the 16 ice core drill sites. Radargrams are 1100 m in depth, spanning the bottom 1000 m of each ice core. Backscatter power color scales are standardized to span 0.5% to 99% of the return power amplitude recorded in the presented depth range. Radar system characteristics can be found in Supplementary Table 1. The depth of the broken climate record, described in Appendix A, is marked at the relevant core sites. The quality of radar scattering at the ice core drill site is color-coded based on categorization as coherent, diffuse and banded, incoherent and laterally homogeneous, incoherent and laterally heterogeneous, or no signal (below the noise floor). (a) Radargrams from Byrd, Dye-3, EDML, Siple Dome, Talos Dome, South Pole, and WAIS Divide exhibit coherent laterally continuous scattering until the noise floor of the radar instrument is reached. Lack of scattering once the instrument reaches the noise floor inhibits interpretation of the quality of the climate record at depth. (b) Radargrams from Camp Century, EDC, GISP2, GRIP, NEEM, Vostok, Dome Fuji, NorthGRIP, and EastGRIP exhibit a variety of incoherent scattering patterns. Incoherent scattering is observed within both continuous climate records at Camp Century, EDC, Vostok, Dome Fuji, NorthGRIP, and EastGRIP, and broken climate records at EDC, GRIP, GISP2, NEEM, Vostok. *Laterally heterogeneous incoherent scattering at GISP2 and GRIP is best observed along the extended 35 km radar transects in Fig. S4.

5. Conclusions

Based on comparison between ice core data and ice-penetrating radar imagery at ice core sites, we show that diffuse and incoherent scattering is often collocated with transitions in the crystal orientation fabric of the ice. Transitions in fabric are a product of the local stress regime, but they are localized by differences in grain size. High concentrations of impurities tend to reduce local grain-size and enhance deformation rates, so where climatically driven variations in impurities change the strength of the ice, one might also expect more abrupt contrasts in fabric that back-scatter radio waves. In this way, fabric controlled

Deleted: 17

Deleted: (except for Taylor Dome where the raw data has been lost)...

Deleted: , Taylor Dome

Deleted: , or bedrock at Taylor Dome,

Deleted: S3

451 scattering may be roughly isochronous, although we show that fabric interfaces do not manifest as abrupt, specular reflectors
452 the way chemically induced layering does in radar imagery.
453

454 In the deep ice, where stresses are high, the age-depth scale is compressed, and global changes in impurity deposition are
455 expressed over narrower depth ranges, we might expect fabric induced scattering to be common. The nature of the fabric
456 transition, and the spatial heterogeneity in the transition, define whether or not the scattering will appear as coherent layering,
457 a diffuse scattering horizon, laterally homogenous incoherent scattering, or laterally heterogeneous incoherent scattering. In
458 addition, ice fluidity contrasts at fabric boundaries facilitate small- and large-scale folding. At small scales (below ~1 m),
459 folding seems to have little impact on existing radar data. But large-scale folding, where present, results in complex scattering
460 targets in the subsurface, and induces significant lateral heterogeneity in the incoherent scattering intensity and complex
461 scattering horizons. Where this is observed at existing ice core sites, it seems indicative of discontinuities in the ice core climate
462 record.
463

464 A final consideration when thinking about fabric induced incoherent scattering is the relationship between permittivity
465 contrasts (as experienced by the propagating radio-wave) and radio-wave polarization. For fabric intensification (for example,
466 a weak single maximum to a strong single maximum fabric) there will be a change in permittivity for all radar polarizations,
467 and scattering will likely appear isotropic. For fabric transitions (for example, from a girdle to a single maximum fabric) it is
468 possible for some polarizations to exhibit scattering and others to have low backscatter or apparent echo free zones. This
469 anisotropic character merits further study at places like Siple Dome, EDML, EastGRIP, and Vostok, where girdles are seen in
470 the deep ice.
471

472 As is true for discussions of the “echo free zone”, we show that conversations about the “basal layer” observed in Greenland
473 and Antarctica must start from the understanding that deep scattering (or its absence) depends on system characteristics and
474 physical properties of the ice. Using only amplitude information to diagnose the source of scattering is therefore inherently
475 limited, not just by the non-unique nature of geophysical imaging (both echo free zones and deep incoherent scattering could
476 arise from multiple mechanisms) but also due to subjective choices made during image processing. Future surveys with phase-
477 coherent data should augment amplitude analysis with along-track direction-of-arrival analysis to get a quantitative measure
478 of specularity (as in Heister and Scheiber, 2018). But from the historical data, we show that a common mechanism for
479 incoherent scattering in deep ice is transition in ice crystal fabric. We find that qualitative differences in the nature of incoherent
480 scattering can aid in evaluating the suitability of future ice core sites. But most importantly, we hope to emphasize that
481 incoherent scattering is signal, not noise, and more work should be done to better interpret this often overlooked component
482 of radar imagery.

Deleted: Both echo free zones and deep incoherent scattering could arise from multiple mechanisms

Commented [NH1]: Heister, A. & Scheiber, R. Coherent large beamwidth processing of radio-echo sounding data. *The Cryosphere* 12, 2969–2979 (2018).

Deleted: w

486 **6. Data Availability**

487 The radar data and associated metadata used in this analysis is available in the accompanying data dictionary

488 (<https://doi.org/10.7910/DVN/JAQJWZ>).

489 **7. Author Contribution**

490 EM synthesized data from the literature on physical and chemical properties of ice cores and identified radar data from CReSIS,

491 BAS, UT, UW, and AWI. All authors contributed to study design, radargram interpretation, figure creation, and writing of

492 manuscript.

493 **8. Competing Interests**

494 The authors declare that they have no conflict of interest.

495 **9. Acknowledgements**

496 This work was funded through the Center for Oldest Ice Exploration (NSF-2019719). It also represents an aggregation of a

497 tremendous amount of work from previous scholars studying ice cores, and we would like to thank those communities and

498 encourage suggestions from those scholars for new ways to connect ice penetrating radar to measurable ice core quantities.

499

500 **Appendix A. Known Layer Disturbances and Ice Core Continuity Problems**

501 Of the cores studied, 6 show only minor signs of layer disturbances, and contain a continuous climate record through the full
502 depth range of the ice core. Those are EastGRIP, Dome Fuji, NorthGRIP, SPICEcore, and WAIS Divide. Of the other 10 cores,
503 5 have well identified breaks in their climate record, and 4 are likely discontinuous (although the exact stratigraphic break is
504 not well identified), and 1 has conflicting observations of discontinuity. A full list of the ice core data used for these
505 observations, including the oldest age of the continuous climate record, can be found in Fig. S5 and Supplementary Table 2.

506 Here, we describe the observational basis for claims of both continuous and broken climate records.

507 **A.1 Cores with Clear Evidence of Stratigraphic Discontinuities**

508 *(Alphabetically: EDML, GRIP, GISP2, NEEM, Talos Dome, Vostok)*

509 **EPICA (European Project for Ice Coring in Antarctica) Dronning Maud Land, EDML (Length: 2774 m | Break: 2417**
510 **m | Percentage Disturbed: 12.9%):** The chronology called EDML1 has been established for the top 2417 m of the EDML
511 ice core. The top 2366 m of the core is matched to the EDC3 chronology using volcanic signatures (dielectric profiling (DEP),
512 SO₄ concentrations, and electrolyte conductivity measurements) (Ruth et al., 2007). Three tie points between the EDC3
513 chronology and EDML core are matched between 2366 and 2415 m using insoluble dust concentrations, $\delta^{18}\text{O}$, and δD , however
514 these matches are considered uncertain with estimated errors up to several thousand years (Ruth et al., 2007). Macrostructure
515 analysis of linescan images between 2400 and 2500 m shows evidence of large-scale folding (Faria et al., 2010).

517 **Greenland Ice Core Project, GRIP (Length: 3029 m | Break: ~2750 m | Percentage Disturbed: 9.2%) and Greenland**
518 **Ice Sheet Project Two, GISP2D (Length: 3053.4 m | Break: ~2750 m | Percentage Disturbed: 9.9%):** CH₄ and $\delta^{18}\text{O}_{\text{atm}}$
519 data from both GRIP and GISP2 show evidence of stratigraphic disturbance in the bottom 10% the ice cores. Above 2750 m
520 CH₄ and $\delta^{18}\text{O}_{\text{atm}}$ values vary synchronously between GRIP and GISP2, but below 2750 m, the chemical profiles diverge,
521 showing large and significant fluctuations which are not present in the undisturbed ice from the Vostok 3G core (Chappellaz
522 et al., 1997).

524 **North Greenland Eemian Ice Drilling, NEEM (Length: 2540 m | Break: 2209.6 m | Percentage Disturbed: 13%):** At
525 NEEM, an abrupt discontinuity in the $\delta^{18}\text{O}_{\text{ice}}$ at 2209.6 m marks the end of synchronization with the NorthGRIP GICC05
526 extended timescale. Additional discontinuities in the $\delta^{18}\text{O}_{\text{ice}}$ subdivide the bottom 13% of the core into six zones of disturbed
527 stratigraphy. These correspond with similar shifts in other atmospheric gas measurements (CH₄, $\delta^{18}\text{O}_{\text{atm}}$, N₂O, $\delta^{15}\text{N}$ of N₂).
528 Within the upper five zones, the layering is thought to be unbroken (based on continuous records of N₂O, $\delta^{15}\text{N}$ of N₂, dust, or
529 electrical properties), with timescales for each of the upper five zones reconstructed by synchronizing NEEM $\delta^{18}\text{O}_{\text{atm}}$ and CH₄
530

Deleted: Taylor Dome,

Deleted: 11

Deleted: 6

Deleted: a

535 profiles with NorthGRIP and EDML records. The timescales for these zones include inverted, mirrored, and folded ice up to
536 100 m thick (NEEM Community Members, 2013).

537

538 **TALos Dome Ice CorE, TALDICE (Length: 1620 m | Break: 1548 m | Percentage Disturbed: 4.4%):** At Talos Dome,
539 Crotti et al. identify a break in stratigraphic continuity at 1548 m using analysis of $\delta^{18}\text{O}_{\text{atm}}$, δD , and 81Kr dating, described
540 below (Crotti et al., 2021). TALDICE $\delta^{18}\text{O}_{\text{atm}}$ and δD measurements were matched to the EDC $\delta^{18}\text{O}_{\text{atm}}$ and δD record through
541 visual synchronization through 1548 m depth. Below 1548 m, the amplitude of $\delta^{18}\text{O}_{\text{atm}}$ fluctuations is damped, making
542 synchronization with the EDC record uncertain. Similarly, below 1548 m, the TALDICE δD signal becomes asynchronous
543 with the EDC record. ^{81}Kr dating of three samples below 1548 m depth revealed that ice from 1613 - 1618 m had comparable
544 age to samples from 1559 - 1563 m and 1573 - 1578 m depth, indicating a disturbed age-depth relationship.

545

546 **Vostok 5G-5 (Length: 3658 m | Break: 3311 m | Percentage Disturbed: 9.5%):** The stratigraphy in the bottom 9% of the
547 Vostok 5G core is divided between 228 m of disturbed meteoric ice, and 119 m of accreted lake ice. In the upper part of the
548 disturbed meteoric ice, the lack of depth-shift between $\delta\text{D}_{\text{ice}}$ and gas measurements (CO_2 and CH_4) is interpreted by Souchez
549 et al. as evidence of folding and intermixing (Souchez et al., 2002). Observations of ash layers with depth-varying inclinations
550 supports interpretation of large-scale folding. In the lower part of the disturbed meteoric ice, damped variation of $\delta\text{D}_{\text{ice}}$ and
551 trace impurity distributions (Na^+ , Cl^- , non-sea salt Mg^{++} and Ca^{++}), physical observations of interbedded fine-grained
552 (presumably glacial) and coarse-grained (presumably interglacial) ice, and the presence of bed material in the bottom 100 m
553 of the disturbed meteoric ice, is interpreted as further evidence for stratigraphic deformation (Lipenkov and Raynaud, 2015;
554 Souchez et al., 2002). At 3538 m depth, the transition between meteoric and accreted ice is apparent from the $\delta\text{D}_{\text{ice}}/\delta^{18}\text{O}$
555 fingerprint of freezing processes (Jouzel et al., 1999). At this depth, sudden transitions to lower total gas content, increased
556 crystal size, low ECM values, increased $\delta\text{D}_{\text{ice}}$, and decreased deuterium excess, provide further evidence for the
557 meteoric/accreted ice transition (Jouzel et al., 1999).

558 **A.2 Cores that Likely Contain Stratigraphic Discontinuities or Conflicting Observations of Discontinuity**

559 *(Alphabetically: Byrd, Camp Century, EPICA Dome C, Dye-3, Siple Dome)*

560

561 **Byrd Station '68, BYRD 68 (Length: 2164 m | Break: 2135-2144 m | Percentage Disturbed: ~1%):** A chronology for the
562 upper ~99% (2144 m) of the Byrd core has been established by synchronizing Byrd, GRIP, and GISP2 CH_4 profiles (Blunier
563 and Brook, 2001). Gas volume measurements from the bottom 10 m of the core (2154 - 2164 m) suddenly approach zero at
564 4.83 m above the bed, revealing the transition between meteoric ice and accreted subglacial meltwater (Gow et al., 1979). The
565 bottom 4.83 m of non-meteorice ice contain horizontal bands of basal debris including sand, clay, and pebbles as large as 8 cm
566 in diameter (Gow et al., 1979). Grootes et al. 2001 observe that the Byrd $\delta^{18}\text{O}$ record becomes asynchronous with Taylor Dome
567 and Vostok record around 2135 m.

568

569 **Camp Century, CC 63-66 (Length: 1387.4 m | Break: ~1350 m | Percentage Disturbed: 2.7%):** The integrity of the Camp
570 Century climate record is uncertain below 1310 m depth where $\delta^{18}\text{O}$ profiles of Camp Century, GRIP, and GISP2 become
571 asynchronous (Johnsen et al., 2001). Correlation of a smoothed Camp Century $\delta^{18}\text{O}$ profile with benthic foraminifera record
572 from deep sea core RC11-120 provides a tentative extension of the chronology through about 1330 m, the depth of the
573 inflection point associated with Marine Isotope Stage (MIS) 5d (Dansgaard et al., 1985). A dramatic cold event at 1340 m is
574 associated with a similar $\delta^{18}\text{O}$ fluctuation in the disturbed section of the GRIP core at 2800 m (Johnsen et al., 2001). Johnsen
575 et al. describe dramatic fluctuations in $\delta^{18}\text{O}$ below Greenland Interstadial (GI) 23 in the GRIP, GISP2, and Camp Century
576 cores which are not represented in the continuous $\delta^{18}\text{O}$ signal from Vostok (Chappellaz et al., 1997).

577

578 **EPICA Dome C, EDC99 (Length: 3260 m | Potential Break: ~3200 m | Percentage Disturbed: ~1.8%):** The continuity of
579 the upper 98% (3200 m) of the EDC99 core is evidenced primarily through matching of $\delta\text{D}_{\text{ice}}$ to the deep-sea benthic $\delta^{18}\text{O}$
580 record (Jouzel et al., 2007). Additional matching of enhanced ^{10}Be deposition to Matuyama-Brunhes geomagnetic reversal
581 between 3160 and 3170 m (Jouzel et al., 2007) and matching of CO_2 and CH_4 profiles to MIS18 and 19 between 3160 and
582 3185 m further support the continuity of the upper 98% of the core. Below 3200 m, there is contradictory evidence about the
583 continuity of the climate record. Measurements of δD , total air content, gas composition, and dust content suggest continuity
584 to bedrock, while $\delta^{18}\text{O}_{\text{atm}}$, visible inclusions, length of the glacial period, and variability of chemical species distribution
585 suggest altered stratigraphy (Tison et al., 2015).

586

587 **DYE-3, DYE3 79-81 (Length: 2037 m | Break: 1940 m | Percentage Disturbed: 4.8%):** At DYE-3, the continuity of the
588 climate signal is lost between 1900 and 1987 m. Initially, Dansgaard et al. 1982 correlated fluctuations between the $\delta^{18}\text{O}$
589 measurements at DYE-3 and Camp Century through 1987 m depth. Between 1987 and 2010 m, DYE-3 $\delta^{18}\text{O}$ values are quasi-
590 constant, and interpreted as evidence of folded layers. Later, comparison of the $\delta^{18}\text{O}$ values between DYE-3 and GRIP led
591 Johnsen et al., 2001 to identify Greenland Interstadial (GI) 8 at 1900 m as the last undisturbed match point between the two
592 records. However, Johnsen et al. would still identify two match points in the deeper ice: GI 12 (~1925 m) and GI 14 (~1940
593 m). Recent analysis of $\delta^{15}\text{N}-\text{N}_2$ and CH_4 gas records may suggest stratigraphic disturbance beginning at 1895 m depth (Buizert
594 et al., 2024). Since the scale of the gas record disturbances has not yet been quantified, in our analysis we have used 1940 m
595 as the depth of the broken climate record. CO_2 and CH_4 measurements of the bottom 27 m of silty ice have been used to
596 identify 4 distinct zones of highly deformed basal ice (Verbeke et al., 2002).

597

598 **Siple Dome A, SDMA (Length: 1004 m | Break: ~800 m | Percentage Disturbed: ~20%):** The integrity of the Siple Dome
599 climate record is uncertain in the bottom 200 m of the core, however a precise onset depth for the disturbed ice is poorly
600 constrained. A chronology for the 514 - 854 m section of the core was established by synchronizing Siple Dome, GISP2, and
601 GRIP CH_4 profiles (Brook et al., 2005). Below 854 m, the methane data becomes sparse however a possible chronology has

602 been proposed between 854 and 920 m based on the matching of a single inflection point in the $\delta^{18}\text{O}_{\text{atm}}$ profile of Siple Dome
603 core at 920 m with a corresponding GISP2 $\delta^{18}\text{O}_{\text{atm}}$ inflection point (Brook et al., 2005). Macro and micro-scale physical
604 observations by Gow and Meese suggest an interrupted climate record by 800 m depth, summarized here (Gow and Meese,
605 2007). Between 560 and 800 m, sequences of inclined layering occasionally surpassing 10 degrees as well as reversed dips are
606 observed. Below 800 m the core is highly fractured, limiting any further observations of layer structure. Around 700 m, the c-
607 axis fabric shifts suddenly to a single maximum corresponding to a stress regime dominated by strong horizontal shear. Around
608 800 m, the c-axis fabric shifts back to a multi-maxima fabric.

609 **A.3 Cores with No Significant Break in Continuity**

610 *(Alphabetically: EastGRIP, Dome Fuji, NorthGRIP, SPICEcore, WAIS Divide)*

611
612 **East Greenland Ice Core Project, EastGRIP (Length: 2663 m):** Initial assessment of the continuity of the EastGRIP climate
613 record has been performed through synchronization of DEPs and ECMs to NEEM and NGRIP datasets. These techniques have
614 been used to establish the GICC05-EGRIP-1 timescale for the upper 1383.4 m of the core (Mojtabavi et al., 2020). Preliminary
615 comparison of EastGRIP and NGRIP DEP data from the bottom 260 m of the core have been used to construct rough GI tie
616 points through GI 25a (around 2590 m) as well as evidence of the Eemian-Glacial transition at 2618 m (Stoll et al., 2024).
617 Observations of cm-scale overturning folds, boudin-like structures, and inclined layers with opposing tilts are observed
618 periodically between 1375 and 2121 m, the depth of the deepest linescan image (Westhoff, 2021; Weikusat, 2020). Due to the
619 rough synchronization of DEP data below the depths of the linescan images, these physical observations of cm-scale
620 disturbances are not interpreted as significant breaks in the climate record.

621
622 **Dome Fuji, DF2 (Length: 3035.22 m):** The integrity of the Dome Fuji ice core climate record is discussed by the (Dome Fuji
623 Ice Core Project Members, 2017) and summarized here. A chronology for the upper 3028 m of the 3035 m Dome Fuji core
624 was established through the synchronization of $\delta^{18}\text{O}$ records to the EDC δD profile. Physical observations of inclined layers
625 begin at 2400 m and show distinct stepwise increases in inclination: $\sim 8^\circ$ between 2450 - 2600, $\sim 20^\circ$ between 2600 - 2800,
626 $\sim 40^\circ$ between 2800 - 2900, $\sim 45^\circ$ at 2950 m, and $\sim 50^\circ$ at bedrock. Despite the observations of inclined layers, which are
627 attributed to spatially variable basal melt conditions, explicit observations of folded layers were not noted and the synchronicity
628 of the $\delta^{18}\text{O}$ and EDC δD profiles are considered evidence of an intact climate record within the depths of inclined layers.

629
630 **North Greenland Ice Core Project, NorthGRIP2 (Length: 3090 m):** At NorthGRIP, the continuity of the 2544 – 3073 m
631 zone of the 3090 m length core was confirmed by matching NorthGRIP $\delta^{18}\text{O}_{\text{atm}}$ and CH_4 records to EDML and EDML1
632 chronologies (Capron et al., 2010). Depth shift analysis at 2940 m showed the expected shift between $\delta^{15}\text{N}$ and CH_4 vs $\delta^{18}\text{O}$
633 during Dansgaard-Oeschger (DO) 24, and was used to confirm the continuity of the deepest layers (North Greenland Ice Core

Deleted: Taylor Dome,

Deleted:

636 Project Members, 2004). Like at WAIS Divide, small scale stratigraphic disturbances are observed a few hundred meters above
637 bedrock (Svensson, 2005), but are not considered large enough to impact the continuity of the climate record.

638
639 **South Pole Ice Core, SPICEcore, SPC14 (Length: 1500 m | Ice thickness: 2700 m):** Continuity through the end of the core
640 is established through synchronization of CH₄ fluctuations to WAIS Divide ice core (Epifanio et al., 2020). Notably,
641 SPICEcore drilling stopped 1200 m above bedrock.

642
643 ↓
644 **WAIS (West Antarctic Ice Sheet) Divide, WDC06A (Length: 3405 m | Ice thickness: 3455 m):** The continuity of the
645 WAIS Divide core is confirmed above 2850 m by annual layer counting, and below 2850 m via synchronization of WAIS
646 Divide CH₄ measurements to the NorthGRIP δ¹⁸O record and a refined Hulu Cave speleothem δ¹⁸O record (Buizert et al.,
647 2015). Notably, the 3405 m WAIS Divide core ends 50 m above bedrock, so continuity in the uncored 50 m basal unit is not
648 confirmed. Mm-scale or smaller stratigraphic disturbances are observed at 3150 and 3232 m (Fitzpatrick et al., 2014) but are
649 not considered large enough to impact the continuity of the climate record.

650

Deleted: Taylor Dome, M3C1 (Length: 554 m): The continuity of the Taylor Dome core was established through correlation of the CH₄ and δ¹⁸O_{ann} profiles with corresponding GISP2 profiles as well as correlation of the δ¹⁸O profile with the Vostok δD record (Grootes et al., 2001; Steig et al., 1998).

Deleted: The δ¹⁸O inflection point associated with MIS 5e (~130kyrBP) is identified between 526 and 531 m depth. The identification of correlated inflection points continues confidently through 200 kyrBP with a tentative chronology, limited by sample resolution, extending beyond 300 kyrBP (Grootes et al., 2001). ¶

661 **References**

- 662 Alley, R. B., Gow, A. J., Johnsen, S. J., Kipfstuhl, J., Meese, D. A., and Thorsteinsson, T.: Comparison of deep ice cores,
663 *Nature*, 373, 393–394, <https://doi.org/10.1038/373393b0>, 1995.
- 664 Alley, R. B., Gow, A. J., Meese, D. A., Fitzpatrick, J. J., Waddington, E. D., and Bolzan, J. F.: Grain-scale processes, folding,
665 and stratigraphic disturbance in the GISP2 ice core, *J. Geophys. Res. Oceans*, 102, 26819–26830,
666 <https://doi.org/10.1029/96JC03836>, 1997.
- 667 Azuma, N., Wang, Y., Mori, K., Narita, H., Hondoh, T., Shoji, H., and Watanabe, O.: Textures and fabrics in the Dome F
668 (Antarctica) ice core, *Ann. Glaciol.*, 29, 163–168, <https://doi.org/10.3189/172756499781821148>, 1999.
- 669 Bingham, R. G., Bodart, J. A., Cavitte, M. G. P., Chung, A., Sanderson, R. J., Sutter, J. C. R., Eisen, O., Karlsson, N. B.,
670 MacGregor, J. A., Ross, N., Young, D. A., Ashmore, D. W., Born, A., Chu, W., Cui, X., Drews, R., Franke, S., Goel, V.,
671 Goode, J. W., Henry, A. C. J., Hermant, A., Hills, B. H., Holschuh, N., Koutnik, M. R., Leysinger Vieli, G. J.-M. C., Mackie,
672 E. J., Mantelli, E., Martín, C., Ng, F. S. L., Oraschewski, F. M., Napoleoni, F., Parrenin, F., Popov, S. V., Rieckh, T., Schlegel,
673 R., Schroeder, D. M., Siegert, M. J., Tang, X., Teisberg, T. O., Winter, K., Yan, S., Davis, H., Dow, C. F., Fudge, T. J., Jordan,
674 T. A., Kulessa, B., Matsuoka, K., Nyqvist, C. J., Rahmemonfar, M., Siegfried, M. R., Singh, S., Višnjević, V., Zamora, R.,
675 and Zühr, A.: Review Article: Antarctica’s internal architecture: Towards a radiostratigraphically-informed age–depth model
676 of the Antarctic ice sheets, *EGUsphere* [preprint], <https://doi.org/10.5194/egusphere-2024-2593>, 1 October 2024.
- 677 Blunier, T. and Brook, E. J.: Timing of millennial-scale climate change in Antarctica and Greenland during the Last Glacial
678 Period, *Science*, 291, 109–112, <https://doi.org/10.1126/science.291.5501.109>, 2001.
- 679 Brook, E. J., White, J. W. C., Schilla, A. S. M., Bender, M. L., Barnett, B., Severinghaus, J. P., Taylor, K. C., Alley, R. B.,
680 and Steig, E. J.: Timing of millennial-scale climate change at Siple Dome, West Antarctica, during the last glacial period,
681 *Quat. Sci. Rev.*, 24, 1333–1343, <https://doi.org/10.1016/j.quascirev.2005.02.002>, 2005.
- 682 Buizert, C., Cuffey, K. M., Severinghaus, J. P., Baggenstos, D., Fudge, T. J., Steig, E. J., Markle, B. R., Winstrup, M., Rhodes,
683 R. H., Brook, E. J., Sowers, T. A., Clow, G. D., Cheng, H., Edwards, R. L., Sigl, M., McConnell, J. R., and Taylor, K. C.: The
684 WAIS Divide deep ice core WD2014 chronology – Part 1: Methane synchronization (68–31 ka BP) and the gas age–ice age
685 difference, *Clim. Past*, 11, 153–173, <https://doi.org/10.5194/cp-11-153-2015>, 2015.
- 686 Capron, E., Landais, A., Lemieux-Dudon, B., Schilt, A., Masson-Delmotte, V., Buiron, D., Chappellaz, J., Dahl-Jensen, D.,
687 Johnsen, S., Leuenberger, M., Loulergue, L., and Oerter, H.: Synchronising EDML and NorthGRIP ice cores using $\delta^{18}\text{O}$ of
688 atmospheric oxygen ($\delta^{18}\text{O}_{\text{atm}}$) and CH_4 measurements over MIS5 (80–123 kyr), *Quat. Sci. Rev.*, 29, 222–234,
689 <https://doi.org/10.1016/j.quascirev.2009.07.014>, 2010.
- 690 Catania, G. A., Conway, H. B., Gades, A. M., Raymond, C. F., and Engelhardt, H.: Bed reflectivity beneath inactive ice streams
691 in West Antarctica, *Ann. Glaciol.*, 36, 287–291, <https://doi.org/10.3189/172756403781816310>, 2003.
- 692 Chappellaz, J., Brook, E., Blunier, T., and Malaizé, B.: CH_4 and $\delta^{18}\text{O}$ of O_2 records from Antarctic and Greenland ice: a clue
693 for stratigraphic disturbance in the bottom part of the Greenland Ice Core Project and the Greenland Ice Sheet Project 2 ice
694 cores, *J. Geophys. Res.*, 102, 26547–26557, <https://doi.org/10.1029/97JC00164>, 1997.
- 695 Christianson, K., Jacobel, R. W., Horgan, H. J., Alley, R. B., Anandakrishnan, S., Holland, D. M., and DallaSanta, K. J.: Basal
696 conditions at the grounding zone of Whillans Ice Stream, West Antarctica, from ice-penetrating radar, *J. Geophys. Res. Earth*,
697 121, 1954–1983, <https://doi.org/10.1002/2015JF003806>, 2016.

698 Chu, W., Schroeder, D. M., Seroussi, H., Creyts, T. T., and Bell, R. E.: Complex basal thermal transition near the onset of
699 Petermann Glacier, Greenland, *J. Geophys. Res. Earth*, 123, 985–995, <https://doi.org/10.1029/2017JF004561>, 2018.

700 Chung, A., Parrenin, F., Steinhage, D., Mulvaney, R., Martin, C., Cavitte, M. G. P., Lilien, D. A., Veit, H., Taylor, D.,
701 Gogineni, P., Ritz, C., Frezzotti, M., O’Neill, C., Heinrich, M., Dahl-Jensen, D., and Eisen, O.: Stagnant ice and age modelling
702 in the Dome C region, Antarctica, *The Cryosphere*, 17, 3461–3483, <https://doi.org/10.5194/tc-17-3461-2023>, 2023.

703 Crotti, I., Landais, A., Stenni, B., Bazin, L., Parrenin, F., Frezzotti, M., Ritterbusch, F., Lu, Z.-T., Jiang, W., Yang, G.-M.,
704 Fourré, E., Orsi, A., Jacob, R., Minster, B., Prié, F., Dreossi, G., and Barbante, C.: An extension of the TALDICE ice core age
705 scale reaching back to MIS 10.1, *Quat. Sci. Rev.*, 266, 107078, <https://doi.org/10.1016/j.quascirev.2021.107078>, 2021.

706 Dahl-Jensen, D., Gundestrup, N. S., Keller, K., Johnsen, S. J., Gogineni, S. P., Allen, C. T., Chuah, T. S., Miller, H., Kipfstuhl,
707 S., and Waddington, E. D.: A search in North Greenland for a new ice-core drill site, *J. Glaciol.*, 43, 300–306,
708 <https://doi.org/10.3189/S0022143000003245>, 1997.

709 Dansgaard, W.: A New Greenland Deep Ice Core, *Science*, 218, 1273–1277, 1982.

710 Dansgaard, W., Clausen, H. B., Gundestrup, N., Johnsen, S. J., and Rygner, C.: Dating and climatic interpretation of two deep
711 Greenland ice cores, in: *Greenland Ice Core: Geophysics, Geochemistry, and the Environment*, vol. 33, edited by: Langway,
712 C. C., Oeschger, H., and Dansgaard, W., American Geophysical Union, Washington, D. C., 71–76,
713 <https://doi.org/10.1029/GM033p0071>, 1985.

714 Dome Fuji Ice Core Project Members: State dependence of climatic instability over the past 720,000 years from Antarctic ice
715 cores and climate modeling, *Sci. Adv.*, 3, <https://doi.org/10.1126/sciadv.1600446>, 2017.

716 Dowdeswell, J. A. and Evans, S.: Investigations of the form and flow of ice sheets and glaciers using radio-echo sounding,
717 *Rep. Prog. Phys.*, 67, 1821–1861, <https://doi.org/10.1088/0034-4885/67/10/R03>, 2004.

718 Durand, G., Svensson, A., Persson, A., Gillet-Chaulc, F., Montagnat, M., and Dahl-Jensen, D.: Evolution of the texture along
719 the EPICA Dome C ice core, *Physics of Ice Core Records II: Papers collected after the 2nd International Workshop on Physics
720 of Ice Core Records*, held in Sapporo, Japan, 68, 91–105, 2009.

721 Eichler, J.: C-axis analysis of the NEEM ice core, Master’s Thesis, Freie Universitat, Berlin, Germany, 63 pp., 2013.

722 Eisen, O., Wilhelms, F., Nixdorf, U., and Miller, H.: Revealing the nature of radar reflections in ice: DEP-based FDTD forward
723 modeling, *Geophys. Res. Lett.*, 30, <https://doi.org/10.1029/2002GL016403>, 2003.

724 Eisen, O., Hamann, I., Kipfstuhl, S., Steinhage, D., and Wilhelms, F.: Direct evidence for continuous radar reflector originating
725 from changes in crystal-orientation fabric, *The Cryosphere*, 1, 1–10, <https://doi.org/10.5194/tc-1-1-2007>, 2007.

726 Epifanio, J. A., Brook, E. J., Buizert, C., Edwards, J. S., Sowers, T. A., Kahle, E. C., Severinghaus, J. P., Steig, E. J., Winski,
727 D. A., Osterberg, E. C., Fudge, T. J., Aydin, M., Hood, E., Kalk, M., Kreutz, K. J., Ferris, D. G., and Kennedy, J. A.: The SP19
728 chronology for the South Pole Ice Core – Part 2: gas chronology, Δ age, and smoothing of atmospheric records, *Clim. Past*, 16,
729 2431–2444, <https://doi.org/10.5194/cp-16-2431-2020>, 2020.

730 Fahnestock, M., Abdalati, W., Joughin, I., Brozena, J., and Gogineni, P.: High geothermal heat flow, basal melt, and the origin
731 of rapid ice flow in Central Greenland, *Science*, 294, 2338–2342, <https://doi.org/10.1126/science.1065370>, 2001.

732 Faria, S. H., Freitag, J., and Kipfstuhl, S.: Polar ice structure and the integrity of ice-core paleoclimate records, *Quat. Sci. Rev.*,
733 29, 338–351, <https://doi.org/10.1016/j.quascirev.2009.10.016>, 2010.

734 Faria, S. H., Weikusat, I., and Azuma, N.: The microstructure of polar ice. Part I: Highlights from ice core research, *J. Struct.*
735 *Geol.*, 61, 2–20, <https://doi.org/10.1016/j.jsg.2013.09.010>, 2014.

736 Faria, S. H., Kipfstuhl, S., and Lambrecht, A.: The EPICA-DML Deep Ice Core: A Visual Record, Springer Berlin Heidelberg,
737 Berlin, Heidelberg, 305 pp., <https://doi.org/10.1007/978-3-662-55308-4>, 2018.

738 Fegyveresi, J. M. and Alley, R. B.: South Pole Ice Core (SPIcecore) Visual Observations [data set],
739 <https://doi.org/10.15784/601088>, 2018.

740 Fitzpatrick, J. J., Voigt, D. E., Fegyveresi, J. M., Stevens, N. T., Spencer, M. K., Cole-Dai, J., Alley, R. B., Jardine, G. E.,
741 Cravens, E. D., Wilen, L. A., Fudge, T. J., and McConnell, J. R.: Physical properties of the WAIS Divide ice core, *J. Glaciol.*,
742 60, 1181–1198, <https://doi.org/10.3189/2014JoG14J100>, 2014.

743 Fudge, T. J., Taylor, K. C., Waddington, E. D., Fitzpatrick, J. J., and Conway, H.: Electrical stratigraphy of the WAIS Divide
744 ice core: identification of centimeter-scale irregular layering, *J. Geophys. Res. Earth Surf.*, 121, 1218–1229,
745 <https://doi.org/10.1002/2016JF003845>, 2016.

746 Fudge, T. J., Hills, B. H., Horlings, A. N., Holschuh, N., Christian, J. E., Davidge, L., Hoffman, A., O'Connor, G. K.,
747 Christianson, K., and Steig, E. J.: A site for deep ice coring at West Hercules Dome: results from ground-based geophysics
748 and modeling, *J. Glaciol.*, 69, 538–550, <https://doi.org/10.1017/jog.2022.80>, 2023.

749 Fujita, S., Maeno, H., Uratsuka, S., Furukawa, T., Mae, S., Fujii, Y., and Watanabe, O.: Nature of radio echo layering in the
750 Antarctic Ice Sheet detected by a two-frequency experiment, *J. Geophys. Res.*, 104, 13013–13024,
751 <https://doi.org/10.1029/1999JB900034>, 1999.

752 Gerber, T. A., Lilien, D. A., Nymand, N. F., Steinhage, D., Eisen, O., and Dahl-Jensen, D.: Anisotropic scattering in radio-
753 echo sounding: insights from Northeast Greenland, *EGUsphere* [preprint], <https://doi.org/10.5194/egusphere-2024-2276>, 6
754 September 2024.

755 Gow, A. J. and Meese, D.: Physical properties, crystalline textures and c-axis fabrics of the Siple Dome (Antarctica) ice core,
756 *J. Glaciol.*, 53, 573–584, <https://doi.org/10.3189/002214307784409252>, 2007.

757 Gow, A. J., Epstein, S., and Sheehy, W.: On the origin of stratified debris in ice cores from the bottom of the Antarctic Ice
758 Sheet, *J. Glaciol.*, 23, 185–192, <https://doi.org/10.3189/S0022143000029828>, 1979.

759 Gow, A. J., Meese, D. A., Alley, R. B., Fitzpatrick, J. J., Anandakrishnan, S., Woods, G. A., and Elder, B. C.: Physical and
760 structural properties of the Greenland Ice Sheet Project 2 ice core: a review, *J. Geophys. Res.*, 102, 26559–26575,
761 <https://doi.org/10.1029/97JC00165>, 1997.

762 Grootes, P. M., Steig, E. J., Stuiver, M., Waddington, E. D., Morse, D. L., and Nadeau, M.-J.: The Taylor Dome Antarctic ^{18}O
763 record and globally synchronous changes in climate, *Quat. Res.*, 56, 289–298, <https://doi.org/10.1006/qres.2001.2276>, 2001.

764 Hammer, C. U.: Acidity of polar ice cores in relation to absolute dating, past volcanism, and radio echoes, *J. Glaciol.*, 24, 359-
765 372, <https://doi.org/10.3189/S0022143000015227>, 1980.

766 Hamran, S., Aarholt, E., Hagen, J. O., and Mo, P.: Estimation of relative water content in a sub-polar glacier using surface-
767 penetration radar, *J. Glaciol.*, 42, 533–537, 1996.

768 Harrison, C. H.: Radio echo sounding of horizontal layers in ice, *J. Glaciol.*, 12, 383-397,
769 <https://doi.org/10.3189/S0022143000031804>, 1973.

770 [Heister, A. and Scheiber, R.: Coherent large beamwidth processing of radio-echo sounding data, *The Cryosphere*, 12, 2969–](#)
771 [2979, <https://doi.org/10.5194/tc-12-2969-2018>, 2018.](#)

772 Howat, I. M., Porter, C., Smith, B. E., Noh, M.-J., and Morin, P.: The reference elevation model of Antarctica, *The Cryosphere*,
773 13, 665–674, <https://doi.org/10.5194/tc-13-665-2019>, 2019.

774 Jansen, D., Llorens, M.-G., Westhoff, J., Steinbach, F., Kipfstuhl, S., Bons, P., Grier, A., and Weikusat, I.: Small-scale
775 disturbances in the stratigraphy of the NEEM ice core: observations and numerical model simulations, *The Cryosphere*, 10,
776 [359–370, <https://doi.org/10.5194/tc-10-359-2016>, 2016.](#)

777 Johnsen, S. J., Clausen, H. B., Dansgaard, W., Gundestrup, N. S., Hammer, C. U., and Tauber, H.: The Eem stable isotope
778 record along the GRIP ice core and its interpretation, *Quat. Res.*, 43, 117–124, <https://doi.org/10.1006/qres.1995.1013>, 1995.

779 Johnsen, S. J., Dahl-Jensen, D., Gundestrup, N., Steffensen, J. P., Clausen, H. B., Miller, H., Masson-Delmotte, V.,
780 Sveinbjörnsdóttir, A. E., and White, J.: Oxygen isotope and palaeotemperature records from six Greenland ice-core stations:
781 Camp Century, Dye-3, GRIP, GISP2, Renland and NorthGRIP, *J. Quat. Sci.*, 16, 299–307, <https://doi.org/10.1002/jqs.622>,
782 2001.

783 Jouzel, J. and Masson-Delmotte, V.: Deep ice cores: the need for going back in time, *Quat. Sci. Rev.*, 29, 3683–3689,
784 <https://doi.org/10.1016/j.quascirev.2010.10.002>, 2010.

785 Jouzel, J., Petit, J. R., Souchez, R., Barkov, N. I., Lipenkov, V. Ya., Raynaud, D., Stievenard, M., Vassiliev, N. I., Verbeke,
786 V., and Vimeux, F.: More than 200 meters of lake ice above subglacial Lake Vostok, Antarctica, *Science*, 286, 2138–2141,
787 <https://doi.org/10.1126/science.286.5447.2138>, 1999.

788 Jouzel, J., Masson-Delmotte, V., Cattani, O., Dreyfus, G., Falourd, S., Hoffmann, G., Minster, B., Nouet, J., Barnola, J. M.,
789 Chappellaz, J., Fischer, H., Gallet, J. C., Johnsen, S., Leuenberger, M., Loulergue, L., Luethi, D., Oerter, H., Parrenin, F.,
790 Raisbeck, G., Raynaud, D., Schilt, A., Schwander, J., Selmo, E., Souchez, R., Spahni, R., Stauffer, B., Steffensen, J. P., Stenni,
791 B., Stocker, T. F., Tison, J. L., Werner, M., and Wolff, E. W.: Orbital and millennial Antarctic climate variability over the past
792 800,000 years, *Science*, 317, 793–796, <https://doi.org/10.1126/science.1141038>, 2007.

793 Karlsson, N. B., Binder, T., Eagles, G., Helm, V., Pattyn, F., Lieffering, B. V., and Eisen, O.: Glaciological characteristics in
794 the Dome Fuji region and new assessment for oldest ice, *The Cryosphere*, 12, 2413–2424, [https://doi.org/10.5194/tc-12-2413-](https://doi.org/10.5194/tc-12-2413-2018)
795 [2018](#), 2018.

796 Karlsson, N. B., Razik, S., Hörhold, M., Winter, A., Steinhage, D., Binder, T., and Eisen, O.: Surface accumulation in Northern
797 Central Greenland during the last 300 years, *Ann. Glaciol.*, 61, 214–224, <https://doi.org/10.1017/aog.2020.30>, 2020.

798 Kipfstuhl, S.: Visual Stratigraphy of the NEEM Ice Core with Linescanner [data set],
799 <https://doi.org/10.1594/PANGAEA.743062>, 2009.

800 Kluskiewicz, D., Waddington, E. D., Anandakrishnan, S., Voigt, D. E., Matsuoka, K., and McCarthy, M. P.: Sonic methods
801 for measuring crystal orientation fabric in ice, and results from the West Antarctic Ice Sheet (WAIS) Divide, *J. Glaciol.*, 63,
802 603–617, <https://doi.org/10.1017/jog.2017.20>, 2017.

803 Landais, A., Chappellaz, J., Delmotte, M., Jouzel, J., Blunier, T., Bour, C., Caillon, N., Cherrier, S., Malaizé, B., Masson-
804 Delmotte, V., Raynaud, D., Schwander, J., and Steffensen, J. P.: A tentative reconstruction of the last interglacial and glacial
805 inception in Greenland based on new gas measurements in the Greenland Ice Core Project (GRIP) ice core, *J. Geophys. Res.*
806 *Atm.*, 108, <https://doi.org/10.1029/2002JD003147>, 2003.

Deleted: The Cryosphere Discussions, 9,
<https://doi.org/10.5194/tcd-9-5817-2015>, 2015

809 Langway, C. C., Shoji, H., and Azuma, N.: Crystal size and orientation patterns in the Wisconsin-age ice from Dye 3,
810 Greenland, *Ann. Glaciol.*, 10, 109–115, <https://doi.org/10.3189/S0260305500004262>, 1988.

811 Leysinger Viel, G. J.-M. C., Hindmarsh, R. C. a, and Siegert, M. J.: Three-dimensional flow influences on radar layer
812 stratigraphy, *Ann. Glaciol.*, 22–28, 2007.

813 Lilien, D. A., Steinhage, D., Taylor, D., Parrenin, F., Ritz, C., Mulvaney, R., Martín, C., Yan, J.-B., O’Neill, C., Frezzotti, M.,
814 Miller, H., Gogineni, P., Dahl-Jensen, D., and Eisen, O.: Brief communication: new radar constraints support presence of ice
815 older than 1.5 Myr at Little Dome C, The Cryosphere, 15, 1881–1888, <https://doi.org/10.5194/tc-15-1881-2021>, 2021.

816 Lindzey, L. E., Beem, L. H., Young, D. A., Quartini, E., Blankenship, D. D., Lee, C.-K., Lee, W. S., Lee, J. I., and Lee, J.:
817 Aerogeophysical characterization of an active subglacial lake system in the David Glacier catchment, Antarctica, The
818 Cryosphere, 14, 2217–2233, <https://doi.org/10.5194/tc-14-2217-2020>, 2020.

819 Lipenkov, V. Ya. and Raynaud, D.: The Mid-Pleistocene transition and the Vostok oldest ice challenge, *Ice and Snow*, 55, 95–
820 106, <https://doi.org/10.15356/2076-6734-2015-4-95-106>, 2015.

821 Matsuo, T., Fujita, S., and Mae, S.: Dielectric properties of ice containing ionic impurities at microwave frequencies. *J.*
822 *Phys. Chem. B.*, 101(32), 6219–6222, <https://doi.org/10.1021/jp9631590>, 1997.

823 Millar, D. H. M.: Acidity levels in ice sheets from radio echo-soundings. *Ann. Glaciol.*, 3, 199–203,
824 <https://doi.org/10.3189/S0260305500002779>, 1982.

825 Miyamoto, A., Weikusat, I., and Hondoh, T.: Complete determination of ice crystal orientation using Laue X-ray diffraction
826 method, *J. Glaciol.*, 57, 103–110, <https://doi.org/10.3189/002214311795306754>, 2011.

827 Mojtavavi, S., Eisen, O., Franke, S., Jansen, D., Steinhage, D., Paden, J., Dahl-Jensen, D., Weikusat, I., Eichler, J., and
828 Wilhelms, F.: Origin of englacial stratigraphy at three deep ice core sites of the Greenland Ice Sheet by synthetic radar
829 modelling, *J. Glaciol.*, 68, 799–811, <https://doi.org/10.1017/jog.2021.137>, 2022.

830 Mojtavavi, S., Wilhelms, F., Cook, E., Davies, S. M., Sinnl, G., Skov Jensen, M., Dahl-Jensen, D., Svensson, A., Vinther, B.
831 M., Kipfstuhl, S., Jones, G., Karlsson, N. B., Faria, S. H., Gkinis, V., Kjær, H. A., Erhardt, T., Berben, S. M. P., Nisancioglu,
832 K. H., Koldtoft, I., and Rasmussen, S. O.: A first chronology for the East Greenland Ice-core Project (EGRIP) over the
833 Holocene and last glacial termination, *Clim. Past*, 16, 2359–2380, <https://doi.org/10.5194/cp-16-2359-2020>, 2020.

834 Montagnat, M., Buiron, D., Arnaud, L., Broquet, A., Schlitz, P., Jacob, R., and Kipfstuhl, S.: Measurements and numerical
835 simulation of fabric evolution along the Talos Dome ice core, Antarctica, *Earth and Planetary Science Letters*, 357–358, 168–
836 178, <https://doi.org/10.1016/j.epsl.2012.09.025>, 2012.

837 Montagnat, M., Azuma, N., Dahl-Jensen, D., Eichler, J., Fujita, S., Gillet-Chaulet, F., Kipfstuhl, S., Samyn, D., Svensson, A.,
838 and Weikusat, I.: Fabric along the NEEM ice core, Greenland, and its comparison with GRIP and NGRIP ice cores, *The*
839 *Cryosphere*, 8, 1129–1138, <https://doi.org/10.5194/tc-8-1129-2014>, 2014.

840 Mougnot J., and Rignot E.: Glacier catchments/basins for the Greenland Ice Sheet [data set], *Dryad*,
841 <https://doi.org/10.7280/D1WT11>, 2019.

842 Mulvaney, R., Rix, J., Polfrey, S., Grieman, M., Martin, C., Nehrbass-Ahles, C., Rowell, I., Tuckwell, R., and Wolff, E.: Ice
843 drilling on Skytrain Ice Rise and Sherman Island, Antarctica, *Ann. Glaciol.*, 62, 311–323, <https://doi.org/10.1017/aog.2021.7>,
844 2021.

845 NEEM Community Members: Eemian interglacial reconstructed from a Greenland folded ice core, *Nature*, 493, 489–494,
846 <https://doi.org/10.1038/nature11789>, 2013.

847 North Greenland Ice Core Project Members: High-resolution record of Northern Hemisphere climate extending into the last
848 interglacial period, *Nature*, 431, 147–151, <https://doi.org/10.1038/nature02805>, 2004.

849 Nymand, N. F., Radar investigation of the Northeast Greenland Ice Stream: Deriving the crystal orientation fabric, Ph.D. thesis,
850 University of Copenhagen, Denmark, 130 pp., 2024.

851 Obbard, R. and Baker, I.: The microstructure of meteoric ice from Vostok, Antarctica, *J. Glaciol.*, 53, 41–62,
852 <https://doi.org/10.3189/172756507781833901>, 2007.

853 Oswald, G. K. A., Rezvanbehbahani, S., and Stearns, L. A.: Radar evidence of ponded subglacial water in Greenland, *J.*
854 *Glaciol.*, 64(247), 711–729, <https://doi.org/10.1017/jog.2018.60>, 2018.

855 Peters, M. E., Blankenship, D. D., and Morse, D. L.: Analysis techniques for coherent airborne radar sounding: Application to
856 West Antarctic ice streams, *J. Geophys. Res.*, 110, B06303, <https://doi.org/10.1029/2004JB003222>, 2005.

857 Petit, J. R., Jouzel, J., Raynaud, D., Barkov, N. I., Delaygue, G., Delmotte, M., Kotlyakov, V. M., Legrand, M., Lipenkov, V.
858 Y., Lorius, C., and Saltzman, E.: Climate and atmospheric history of the past 420,000 years from the Vostok ice core,
859 Antarctica, *Nature*, 399, 1999.

860 Porter, C., Morin, P., Howat, I., Noh, M.-J., Bates, B., Peterman, K., Keesey, S., Schlenk, M., Gardiner, J., Tomko, K., Willis,
861 M., Kelleher, C., Cloutier, M., Husby, E., Foga, S., Nakamura, H., Platson, M., Wethington Jr., M., Williamson, C., Bauer,
862 G., Enos, J., Arnold, G., Kramer, W., Becker, P., Doshi, A., D'Souza, C., Cummings, P., Laurier, F., and Bojesen, M.:
863 ArcticDEM, V1 [data set], Harvard Dataverse, <https://doi.org/10.7910/DVN/OHHUKH>, 2018.

864 Raynaud, D., Barnola, J.-M., Souchez, R., Lorrain, R., Petit, J.-R., Duval, P., and Lipenkov, V. Y.: The record for marine
865 isotopic stage 11, *Nature*, 436, 39–40, <https://doi.org/10.1038/43639b>, 2005.

866 Rignot, E., Jacobs, S., Mouginot, J., and Scheuchl, B.: Ice-shelf melting around Antarctica, *Science*, 341(6143), 266–270,
867 <https://doi.org/10.1126/science.1235798>, 2013.

868 Ruth, U., Kaufmann, P., Kipfstuhl, S., Lambrecht, A., Morganti, A., Oerter, H., Parrenin, F., Rybak, O., Severi, M., Udisti, R.,
869 Wilhelms, F., and Wolff, E.: “EDML1”: a chronology for the EPICA deep ice core from Dronning Maud Land, Antarctica,
870 over the last 150 000 years, *Clim. Past*, 2007.

871 Saruya, T., Fujita, S., Iizuka, Y., Miyamoto, A., Ohno, H., Hori, A., Shigeyama, W., Hirabayashi, M., and Goto-Azuma, K.:
872 Development of crystal orientation fabric in the Dome Fuji ice core in East Antarctica: implications for the deformation regime
873 in ice sheets, *The Cryosphere*, 16, 2985–3003, <https://doi.org/10.5194/tc-16-2985-2022>, 2022.

874 Saruya, T., Miyamoto, A., Fujita, S., Goto-Azuma, K., Hirabayashi, M., Hori, A., Igarashi, M., Iizuka, Y., Kameda, T., Ohno,
875 H., Shigeyama, W., and Tsutaki, S.: Development of deformational regimes and microstructures in the deep sections and
876 overall layered structures of the Dome Fuji ice core, Antarctica, *EGU sphere*, 1–48, <https://doi.org/10.5194/egusphere-2023-3146>, 2024.

878 Schroeder, D. M., Blankenship, D. D., Raney, R. K., and Grima, C.: Estimating subglacial water geometry using radar bed
879 echo specularity: application to Thwaites Glacier, West Antarctica, *IEEE Geosci. Remote Sensing Lett.*, 12, 443–447,
880 <https://doi.org/10.1109/LGRS.2014.2337878>, 2015.

881 Schroeder, D. M., Bingham, R. G., Blankenship, D. D., Christianson, K., Eisen, O., Flowers, G. E., Karlsson, N. B., Koutnik,
882 M. R., Paden, J. D., and Siegert, M. J.: Five decades of radioglaciology, *Ann. Glaciol.*, 61, 1–13,
883 <https://doi.org/10.1017/aog.2020.11>, 2020.

884 Souchez, R., Petit, J. R., Jouzel, J., Simões, J., De Angelis, M., Barkov, N., Stievenard, M., Vimeux, F., Sleewaegen, J., and
885 Lorrain, R.: Highly deformed basal ice in the Vostok core, Antarctica, *Geophys. Res. Lett.*, 29,
886 <https://doi.org/10.1029/2001GL014192>, 2002.

887 Stillman, D. E., MacGregor, J. a., and Grimm, R. E.: The role of acids in electrical conduction through ice, *J. Geophys. Res.*
888 *Earth Surf.*, 118, 1–16, <https://doi.org/10.1029/2012JF002603>, 2013.

889 Stoll, N., Weikusat, I., Jansen, D., Bons, P., Darányi, K., Westhoff, J., Llorens, M.-G., Wallis, D., Eichler, J., Saruya, T.,
890 Homma, T., Drury, M., Wilhelms, F., Kipfstuhl, S., Dahl-Jensen, D., and Kerch, J.: EastGRIP ice core reveals the exceptional
891 evolution of crystallographic preferred orientation throughout the Northeast Greenland Ice Stream, *EGUsphere* [preprint],
892 <https://doi.org/10.5194/egusphere-2024-2653>, 2024.

893 Stoll, N., Westhoff, J., Bohleber, P., Svensson, A., Dahl-Jensen, D., Barbante, C., Weikusat, I.: Chemical and visual
894 characterisation of EGRIP glacial ice and cloudy bands within, *The Cryosphere*, 17, 2021–2043, [https://doi.org/10.5194/tc-17-](https://doi.org/10.5194/tc-17-2021-2023)
895 [2021-2023](https://doi.org/10.5194/tc-17-2021-2023), 2023.

896 Svensson, A.: Visual stratigraphy of the North Greenland Ice Core Project (NorthGRIP) ice core during the last glacial period,
897 *J. Geophys. Res.*, 110, <https://doi.org/10.1029/2004JD005134>, 2005.

898 Takata, M., Iizuka, Y., Hondoh, T., Fujita, S., Fujii, Y., and Shoji, H.: Stratigraphic analysis of Dome Fuji Antarctic ice core
899 using an optical scanner, *Ann. Glaciol.*, 39, 467–472, <https://doi.org/10.3189/172756404781813899>, 2004.

900 Thorsteinsson, T., Kipfstuhl, J., and Miller, H.: Textures and fabrics in the GRIP ice core, *J. Geophys. Res. Oceans*, 102,
901 26583–26599, <https://doi.org/10.1029/97JC00161>, 1997.

902 Tison, J.-L., de Angelis, M., Littot, G., Wolff, E., Fischer, H., Hansson, M., Bigler, M., Udisti, R., Wegner, A., Jouzel, J.,
903 Stenni, B., Johnsen, S., Masson-Delmotte, V., Landais, A., Lipenkov, V., Loulergue, L., Barnola, J.-M., Petit, J.-R., Delmonte,
904 B., Dreyfus, G., Dahl-Jensen, D., Durand, G., Bereiter, B., Schilt, A., Spahni, R., Pol, K., Lorrain, R., Souchez, R., and Samyn,
905 D.: Retrieving the paleoclimatic signal from the deeper part of the EPICA Dome C ice core, *The Cryosphere*, 9, 1633–1648,
906 <https://doi.org/10.5194/tc-9-1633-2015>, 2015.

907 Turkeev, A. V., Vasilev, N. I., Lipenkov, V. Y., Bolshunov, A. V., Ekaykin, A. A., Dmitriev, A. N., and Vasilev, D. A.:
908 Drilling the new 5G-5 branch hole at Vostok Station for collecting a replicate core of old meteoric ice, *Ann. Glaciol.*, 62, 305–
909 310, <https://doi.org/10.1017/aog.2021.4>, 2021.

910 Verbeke, V., Lorrain, R., Johnsen, S. J., and Tison, J.-L.: A multiple-step deformation history of basal ice from the Dye 3
911 (Greenland) core: new insights from the CO₂ and CH₄ content, *Ann. Glaciol.*, 35, 231–236,
912 <https://doi.org/10.3189/172756402781817248>, 2002.

913 Wang, Y., Thorsteinsson, T., Kipfstuhl, J., Miller, H., Dahl-Jensen, D., and Shoji, H.: A vertical girdle fabric in the NorthGRIP
914 deep ice core, North Greenland, *Ann. Glaciol.*, 35, 515–520, <https://doi.org/10.3189/172756402781817301>, 2002.

915 Weikusat, I., Kipfstuhl, S., and Lambrecht, A.: Crystal c-axes (Fabric G20) of Ice Core Samples Collected from the EDML
916 Ice Core with Links to Raw Data Files [data set], <https://doi.org/10.1594/PANGAEA.807207>, 2013.

Deleted: Steig, E. J., Brook, E. J., White, J. W. C., Sucher, C. M.,
Bender, M. L., Lehman, S. J., Morse, D. L., Waddington, E. D., and
Clow, G. D.: Synchronous climate changes in Antarctica and the
North Atlantic, *Science*, 282, 92–95,
<https://doi.org/10.1126/science.282.5386.92>, 1998.

922 Weikusat, I., Jansen, D., Binder, T., Eichler, J., Faria, S. H., Wilhelms, F., Kipfstuhl, S., Sheldon, S., Miller, H., Dahl-Jensen,
923 D., and Kleiner, T.: Physical analysis of an Antarctic ice core—towards an integration of micro- and macrodynamics of polar
924 ice, *Phil. Trans. R. Soc. Lond. A*, 375, 20150347, <https://doi.org/10.1098/rsta.2015.0347>, 2017.

925 Weikusat, I., Westhoff, J., Kipfstuhl, S., Jansen, D.: Visual stratigraphy of the EastGRIP ice core (14 m - 2021 m depth, drilling
926 period 2017-2019) [data set]. PANGAEA, <https://doi.org/10.1594/PANGAEA.925014>, 2020.

927 Westhoff, J.: Visual stratigraphy of the EastGRIP ice core: of the lost ice core orientation, deformation structures, extreme
928 warm events, and trapped ancient air, Ph.D. thesis, University of Copenhagen, Denmark, 136 pp., 2021.

929 Wilson, C. J. L., Russell-Head, D. S., and Sim, H. M.: The application of an automated fabric analyzer system to the textural
930 evolution of folded ice layers in shear zones, *Ann. Glaciol.*, 37, 7–17, <https://doi.org/10.3189/172756403781815401>, 2003.

931 Winter, A., Steinhage, D., Arnold, E. J., Blankenship, D. D., Cavitte, M. G. P., Corr, H. F. J., Paden, J. D., Urbini, S., Young,
932 D. A., and Eisen, O.: Comparison of measurements from different radio-echo sounding systems and synchronization with the
933 ice core at Dome C, Antarctica, *The Cryosphere*, 11, 653–668, <https://doi.org/10.5194/tc-11-653-2017>, 2017.

934 Winter, K., Woodward, J., Ross, N., Dunning, S. A., Hein, A. S., Westoby, M. J., Culberg, R., Marrero, S. M., Schroeder, D.
935 M., Sugden, D. E., and Siegert, M. J.: Radar-detected englacial debris in the West Antarctic Ice Sheet, *Geophys. Res. Lett.*,
936 46, 10454–10462, <https://doi.org/10.1029/2019GL084012>, 2019.

937 Wolff, E. W.: Electrical stratigraphy of polar ice cores: principles, methods, and findings, in: *Physics of Ice Core Records*,
938 *International Symposium on Physics of Ice Core Records*. Shikotsukohan, Hokkaido, Japan, 155–171, 2000.

939 Wolff, E. W., Barbante, C., Becagli, S., Bigler, M., Boutron, C. F., Castellano, E., De Angelis, M., Federer, U., Fischer, H.,
940 Fundel, F., Hansson, M., Hutterli, M., Jonsell, U., Karlin, T., Kaufmann, P., Lambert, F., Littot, G. C., Mulvaney, R.,
941 Röthlisberger, R., Ruth, U., Severi, M., Siggaard-Andersen, M. L., Sime, L. C., Steffensen, J. P., Stocker, T. F., Traversi, R.,
942 Twarloh, B., Udisti, R., Wagenbach, D., and Wegner, A.: Changes in environment over the last 800,000 years from chemical
943 analysis of the EPICA Dome C ice core, *Quat. Sci. Rev.*, 29, 285–295, <https://doi.org/10.1016/j.quascirev.2009.06.013>, 2010.